

The composition and nature of the dust shell surrounding the binary AFGL 4106^{*} ^{**}

F.J. Molster¹, L.B.F.M. Waters^{1,2}, N. R. Trams³, H. van Winckel⁴, L. Decin⁴, J. Th. van Loon¹, C. Jäger⁵, Th. Henning⁵, H.-U. Käufel⁶, A. de Koter¹, J. Bouwman¹

¹ Astronomical Institute 'Anton Pannekoek', University of Amsterdam, Kruislaan 403, 1098 SJ Amsterdam, The Netherlands

² SRON Space Research Laboratory, P.O. Box 800, NL-9700 AV Groningen, The Netherlands

³ Astrophysics Division, Space Science Department of ESA, ESTEC, PO Box 299, 2200 AG Noordwijk, The Netherlands.

⁴ Instituut voor Sterrenkunde, K.U. Leuven, Celestijnenlaan 200B, 3001 Heverlee, Belgium

⁵ Astrophysical Institute and University Observatory (AIU), Schillergäßchen 2-3, D-07745 Jena, Germany

⁶ European Southern Observatory, Karl-Schwarzschild-Straße 2, D-85748 Garching bei München, Germany

received 23 februari 1999, accepted 16 June 1999

Abstract. We present infrared spectroscopy and imaging of AFGL 4106. The 2.4-5 μm ISO-SWS spectrum reveals the presence of a cool, luminous star ($T_{\text{eff}} \approx 3750$ K) in addition to an almost equally luminous F star ($T_{\text{eff}} \approx 7250$ K). The 5 – 195 μm SWS and LWS spectra are dominated by strong emission from circumstellar dust. We find that the dust consists of amorphous silicates, with a minor but significant contribution from crystalline silicates. The amorphous silicates consist of Fe-rich olivines. The presence of amorphous pyroxenes cannot be excluded but if present they contain much less Fe than the amorphous olivines. Comparison with laboratory data shows that the pure Mg-end members of the crystalline olivine and pyroxene solid solution series are present. In addition, we find strong evidence for simple oxides (FeO and Al₂O₃) as well as crystalline H₂O ice. Several narrow emission features remain unidentified.

Modelling of the dust emission using a dust radiation transfer code shows that large grains ($\approx 1\mu\text{m}$) must be present and that the abundance of the crystalline silicates is between 7 and 15% of the total dust mass, depending on the assumed enstatite to forsterite ratio, which is estimated to be between 1 and 3. The amorphous and crystalline dust components in the shell do not have the same temperature, implying that the different dust species are not thermally coupled. We find a dust mass of $\approx 3.9 \cdot 10^{-2} M_{\odot}$ expelled over a period of $\approx 4 \cdot 10^3$ years for a distance of 3.3 kpc. The F-star in the AFGL 4106 binary is likely a post-red-supergiant in transition to a blue supergiant or WR phase.

Send offprint requests to: F.J. Molster: frankm@astro.uva.nl

^{*} Based on observations with ISO, an ESA project with instruments funded by ESA Member States (especially the PI countries: France, Germany, the Netherlands and the United Kingdom) and with the participation of ISAS and NASA

^{**} Based on observations collected at the European Southern Observatory, La Silla, Chile

Key words: Infrared: stars – Stars: supergiants – Stars: mass loss – Stars: binaries: spectroscopic – Stars: circumstellar matter – Stars: individual: AFGL 4106

1. Introduction

Late stages of evolution of both low and high-mass stars are characterized by high mass-loss in a slow and dusty outflow. Low- and intermediate-mass stars (up to $8 M_{\odot}$) will lose a significant amount of their initial mass on the Asymptotic Giant Branch (AGB). More massive stars will lose their hydrogen-rich envelopes during a red supergiant (RSG) phase. The mass-loss rates can be as high as $10^{-4} M_{\odot}/\text{yr}$ for the low-mass stars and up to $10^{-3} M_{\odot}/\text{yr}$ for the high-mass stars. Low and intermediate mass objects evolve to the blue part of the HR diagram after the entire H-rich envelope has been exhausted, and a planetary nebula (PN) is formed. High mass stars either explode as a supernova while they are red supergiants, or they evolve to the blue part of the HR diagram to become a population I Wolf-Rayet (WR) star before ending their live.

The evolution of transition objects, i.e. stars that are in a rapid phase of evolution between the red and blue part of the HR diagram is not very well known. It is clear however, that mass loss plays an important role in determining evolutionary timescales. Remnants of previous mass-loss phases are still in the vicinity of the star in the form of detached dust shells. Infrared observations clearly reveal the existence of these dust shells and the study of the Circum Stellar Environment (CSE) provides essential information about mass-loss history and consequents of evolution.

The infrared-bright object AFGL 4106 (= IRAS 10215-5916) was classified as a transition object by Hrivnak et al. (1989, hereafter

HKV) based on its IRAS colours. Some confusion exists in the literature about its identification. HKV quote Bidelman, who claim that IRAS 10215-5916 is equal to CoD -58°3221. Apparently, this has sometimes been mistaken in the literature as CPD -58°3221 and therefore HD 303822 (e.g. in the Tycho catalogue). The correct identifications should be HD 302821 and CPD -58°2154.

The central star was classified as a G2 supergiant by García-Lario et al. (1994). The combination of a cool central star with low surface gravity and a relatively warm (i.e. young) detached dust shell is typical for transition objects. García-Lario et al. (1994) found double-peaked [N II] lines in the optical spectrum, which they thought to originate from an expanding envelope. The presence of the [N II] is surprising given the spectral type of this object. From the separation between the two peaks they found an expansion velocity of $v_{\text{exp}} = 17 \pm 2 \text{ km s}^{-1}$, which is quite reasonable for an AGB-wind. The expansion velocity of the detached shell was also measured in the CO (J= 1–0) rotational line and was found to be about 40 km s^{-1} (Josselin et al. 1998). This is high for a low mass AGB star and suggests a massive progenitor. The difference with the [N II] line is remarkable and is probably related to the extended nature of the [N II] emitting region (see van Loon et al., in prep.).

The distance and luminosity of AFGL 4106 are uncertain, which makes it hard to decide directly whether the progenitor was an AGB star or a RSG. The luminosity of $L_x/L_\odot \approx 10^4 \times d^2$ (with d in kpc), suggests that it is a luminous object, which until 2 kpc is a post-AGB star, however if this object is located at a larger distance a post-RSG nature cannot be excluded. We will present evidence that AFGL 4106 is likely a post-RSG. The optical to sub-millimetre energy distribution of AFGL 4106 was analysed in detail by HKV and Gürtler et al. (1996, hereafter GKH). Both studies find a very high mass loss which recently stopped, however with rather different density distributions in the shell.

AFGL 4106 was selected for observations with the Infrared Space Observatory (ISO) in the guaranteed time of the Short Wavelength Spectrometer (SWS) consortium because of its classification as a transition object, and because of its very high infrared flux levels. The high-quality ISO data allow a detailed determination of the dust composition and its distribution in the circumstellar shell, which may yield new insight in the origin and evolution of this remarkable object. Waters et al. (1996) studied the 30-45 μm SWS spectrum of AFGL 4106 and discovered weak narrow emission bands that can be attributed to crystalline silicates. Here we present a full inventory of the solid state emission bands and their identification. For the first time a full radiative transfer model of a CSE including crystalline silicates is presented.

This paper is organised as follows; In Sect. 2 we report on the observations and we discuss the data reduction procedures. In Sect. 3 we present the stellar near in-

Nr.	Instrument + Observing mode	Date	orbit	t_{obs} (sec)
I	SWS AOT01 speed 1	16-01-96	60 (PV)	1172
II	SWS AOT01 speed 2	29-02-96	104	1944
III	LWS 01	29-02-96	104	509
IV	SWS AOT01 speed 3	22-07-96	249	3486

Table 1. ISO observing log for AFGL 4106 (PV = Performance Verification phase)

frared spectrum (2.4 – 5 μm), which shows evidence for the binary nature of this object. In Sect. 4 the infrared excess at 5 – 195 μm , caused by the dust shell, is analyzed. We identify the dust composition using the different solid state features detected in this part of the spectrum. In Sect. 5 we present a radiative transfer fit to the spectrum. In Sect. 6 we discuss the results of this paper and in Sect. 7 we summarize our main conclusions.

2. The observations and data reduction

2.1. ISO observations

Spectra of AFGL 4106 were obtained using the Infrared Space Observatory (ISO, Kessler et al. 1996). Three spectra were taken with the Short Wavelength Spectrometer (SWS, de Graauw et al. 1996) and one with the Long Wavelength Spectrometer (LWS, Clegg et al. 1996, Swinyard et al. 1996). An overview of the ISO observing log can be found in Table 1. Part of spectrum II has already been shown in Waters et al. (1996). Because of its better signal to noise, we will use spectrum IV for our discussion in this paper, but information from the other spectra has been used in the reduction of spectrum IV.

2.1.1. SWS

The SWS spectra (2.36 – 45.3 μm) consist of 12 sub-spectra with slightly overlapping wavelength coverage and each observed by 12 detectors. Each spectrum is scanned twice, the so called up- and down-scan (de Graauw et al. 1996). The spectra were reduced using the SWS off-line analysis pipeline, version 6.0. For a description of flux and wavelength calibration procedures, we refer to Schaeidt et al. (1996) and Valentijn et al. (1996). In the reduction process the calibration files available in April 1998 were used. Judging from the overlap regions of the different sub-bands, further improvement is still possible, but will not influence the overall conclusions of our results.

The main fringes in the 12.0 – 29.5 μm part of the spectrum were removed using the InterActive (IA) data reduction package routine *fringes*. Major irregularities due to glitches and large drops or jumps in each detector were removed by hand. A comparison between the different detectors scanning the same wavelength region was used to determine the location of such jumps. Detectors with a

poor performance at the time of observations were removed.

Several procedures were performed on each sub-band separately to combine the 12 detectors. A sigma clipping procedure was used to remove deviating points. The flux level of the 12 detectors was brought to the average level of the 12 detectors. Finally each sub-spectrum was rebinned to a resolution of $\lambda/\Delta\lambda = 750$.

The individual sub-spectra, when combined into a single spectrum, can show jumps in flux levels at band edges due to imperfect flux calibration or dark current subtraction. Based on the observed jumps, downwards with increasing aperture size, we assume that the flux differences are not due to the significant difference in beam size. Indeed, our ground-based $10\ \mu\text{m}$ image (see Sect. 2.2) shows an angular size well within the SWS apertures. We have adjusted the different subbands, according to the expected source of discrepancy, to form a continuous spectrum. Note that all the shifts are well within the photometric absolute calibration uncertainties (Schaeidt et al. 1996). The $29.5 - 31\ \mu\text{m}$ section is severely affected by memory effects of the detectors. Therefore we have removed this part from the final spectrum.

In Fig. 1 we show the final SWS spectrum and we compare this to the original (without band matching) data of spectrum IV. A comparison of the final SWS spectrum with the original data of spectrum II gives a match of similar quality.

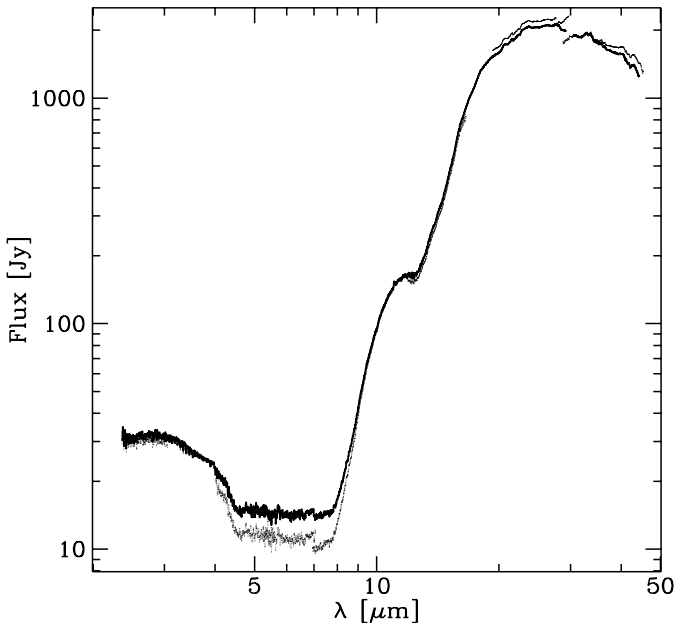


Fig. 1. The final SWS spectrum (thick line), with the different sub-bands attached to each other, compared with the original outcome of the data reduction (dots).

2.1.2. LWS

Spectrum III is an LWS01 full spectral scan ($43 - 195\ \mu\text{m}$). The spectrum was sampled with one point per spectral resolution element using fast scanning. An off-set position spectrum was also taken with the same instrumental parameters, in order to correct for background contributions. The spectrum was reduced using the LWS off-line analysis pipeline, version 6.0. See Table 1 for an overview of the observing mode and date of observation.

The Auto Analysis results of both source and background spectrum were then processed using the ISO Spectral Analysis Package (ISAP). First a median clipped average was calculated of all the spectral scans for one detector. These averaged scans were then fitted together using the scan on the LW1 detector as reference. The resulting spectrum was rebinned to a standard wavelength scale with a resolution of 250 using a flux conserving rebinning routine. Finally, the on-source and off-source spectrum were subtracted. The final SWS + LWS spectrum is presented in Fig. 2.

2.1.3. Comparison with IRAS data

In Fig. 2 we show the complete spectrum together with the IRAS broad band fluxes. We compared the resulting $2.4 - 195\ \mu\text{m}$ spectrum with IRAS data by convolving the ISO spectrum with the IRAS photometric band transmission curves (IRAS explanatory supplement 1988), the resulting fluxes are given in Table 2.

Band (μm)	IRAS-flux (Jy)	Folded ISO-flux (Jy)
12	200.8	169
25	1755	1883
60	851.8	910
100	181.1	283

Table 2. The comparison with the IRAS broadband flux density

The differences found for the 25 and $60\ \mu\text{m}$ flux densities are well within the error that IRAS, SWS and LWS quote for their flux uncertainty. This also holds for the $12\ \mu\text{m}$ flux density, however one should realize that discrepancies in this wavelength regime might be related to the memory effects found in band 2C both for this source (as was found as a difference in the up- and down-scan) as well as in the calibration sources.

The $100\ \mu\text{m}$ IRAS flux density (181.1 Jy) is considerably lower than the flux density in the LWS spectrum (283 Jy) and is outside the errors quoted for IRAS and LWS. We have inspected the raw IRAS data covering the position of AFGL 4106 for bad scans or steep background gradients, which may cause the difference between both

observations. We found no bad scans but there is a conspicuous gradient in the galactic background radiation. However, the IRAS $100\ \mu\text{m}$ flux is corrected for this background. Although the contribution of the background to the LWS continuum flux was found to be minor, the presence of the [C II] line at $158\ \mu\text{m}$, likely to be of interstellar origin, in the continuum subtracted spectrum suggests that the background has not been subtracted correctly. At present, the difference between IRAS $100\ \mu\text{m}$ and LWS is not understood. In Fig. 2, we also show the comparison of the IRAS Low Resolution Spectrograph (LRS) and the final spectrum. The agreement of the shape and flux levels of the LRS and the SWS spectra is satisfactory.

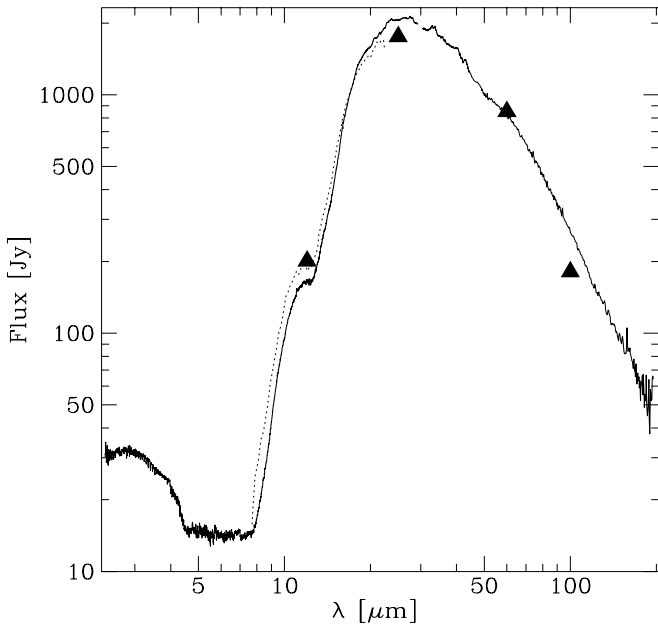


Fig. 2. The final SWS and LWS spectrum of AFGL 4106 (solid line) compared with the IRAS-LRS (dotted line) spectra and the IRAS broad band fluxes (triangles)

2.2. $10\ \mu\text{m}$ imaging at the ESO 3.6m telescope

On 23 February 1994 we used the mid-infrared camera TIMMI (see Käufel et al. (1994) for a description of the instrument) at the ESO 3.6 m telescope on La Silla, Chile, to image AFGL 4106. We used a broad band N filter, centered at $10.1\ \mu\text{m}$. Standard infrared techniques were used, i.e. chopping and nodding with a throw of $23.5''$, somewhat larger than the $21.55''$ field of view. We integrated for 31 minutes on the source. We chose a small pixel scale of $0.336''$ to avoid undersampling of the Point Spread Function (PSF). We observed the standard stars α Hya, ϵ Mus and α Car, to allow for absolute flux calibra-

tion and to derive the PSF (FWHM $\approx 1.2''$) of the telescope plus instrument. We reached the diffraction limit of $0.6''$ by applying a deconvolution algorithm (Lucy 1974) within the MIDAS reduction software package. This deconvolution method has as drawback that it focuses the noise in the background, which is therefore quite spiked. The deconvolved image is shown in Fig. 3. The integrated

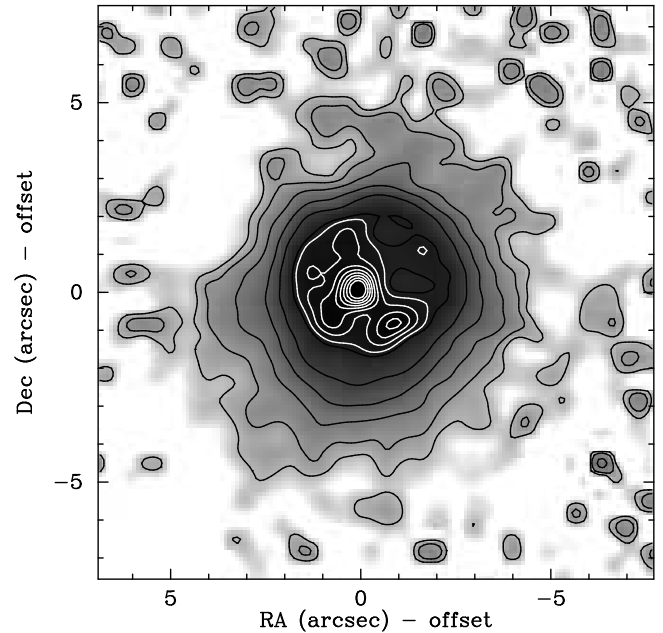


Fig. 3. A logarithmic scale plot of the N-band image of AFGL 4106. The black line contours start at $\sigma = 1$ and are steps of factors 3, the white line start at $\sigma = 300$ and increase in steps of 100 up to 1000. North is up and East is to the left.

instrumental

N-band magnitude (not corrected for color differences etc.) is $N = -1.19 \pm 0.05$. This corresponds to ≈ 120 Jy. The convolution of the N-band sensitivity with the ISO spectrum gives a flux of 100 Jy. The difference between both flux levels is probably caused by detector memory effects in the ISO band 2C wavelength region, and by the slightly extended nature of the nebula. The brightest, unresolved emission peak in the image is likely to be centered on the central object. The nebula, especially the outer parts, seems to have an oval to box-like shape. The inner part of the emission complex is characterized by structure on (sub-)arcsecond scale in the form of local enhancements of $10\ \mu\text{m}$ emission. Whether this also reflects a clumpy density structure is not certain. The North-West part of the nebula is fainter compared to the rest of the nebula at $10\ \mu\text{m}$, and seems slightly more extended. The whole nebula and especially the inner part has a North-West – South-East symmetry axis. The unresolved central peak contains roughly 13% of the total flux, which is about 15

Jy. The total emission extends out to $\approx 5''$ from the center.

An arc of H α emission, extending from roughly North-East to South-West clockwise, has been found (van Loon et al., in prep.), and is located just outside the edge of the extended dust emission in the N-band. This arc coincides with the low surface brightness emission region in the N-band image.

3. The 2.4 – 5 μm part of the spectrum; A binary revealed

The spectral energy distribution (SED) can naturally be divided into two parts. For wavelengths shorter than 5 μm the photosphere radiation dominates the spectrum. Above 5 μm the thermal radiation of the dust dominates the spectrum. This IR-excess will be discussed in Sect. 4. Here, we will present evidence that the central object is a *binary* system, consisting of an M and A-F type star of almost equal luminosity.

The 2.4–5 μm part of the spectrum is shown in Fig. 4. It is dominated by strong absorption from several band heads of ro-vibrational molecular bands, such as the CO first overtone and fundamental, the SiO first overtone, H $_2\text{O}$ (ν_1 and ν_3) and OH fundamental. The strength and

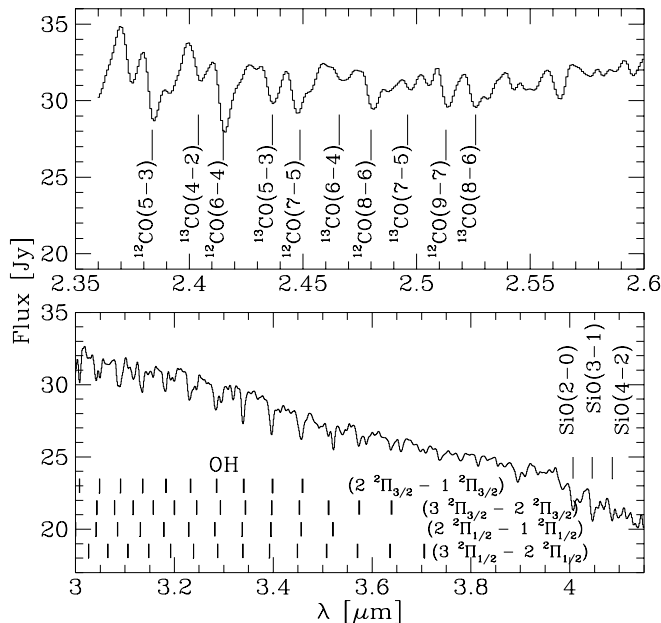


Fig. 4. Ro-vibrational band heads of different molecular species, proving the existence of a cool companion to HD 302821

excitation levels of these bands are not compatible with those expected for a G-type supergiant spectrum, but suggest a cooler star. From the strength and the level of the first

overtone ro-vibrational ^{12}CO bands we derived a temperature of ≈ 4000 K (see e.g. α -Boo in Decin et al. 1997). This high temperature together with the required column density cannot be caused by circumstellar gas in a detached (dusty) envelope. Also the presence of the high excitation lines of gas-phase SiO, which cannot be in a dusty envelope, suggests that we are dealing with a cool star. Meanwhile van Winckel et al. (in prep.) took a high resolution spectra of AFGL 4106 in the optical and around 1 μm and found a warm star of $T \approx 7000 - 7500$ K, dominating in the optical and clear evidence of both the warm and the cool star around 1 μm , where both stars appear to be equally luminous.

In order to verify the binary hypothesis, we have combined the optical and near-IR photometry of AFGL 4106 (HKV, García-Lario et al. 1994, 1997) together with our ISO data. We used Kurucz (1991) model atmospheres to fit the broad-band photometry up to 2.2 μm . This ensures that the fit is not contaminated by dust emission. For our fitting procedure we assumed that the mean interstellar extinction law can be used to describe both the circumstellar and the interstellar dust extinction. We will come back to this point in Sect. 5.2. We were not able to fit the data with a single star, but found a good fit if we assumed a binary. A best fit was found with temperatures of $7250 \pm 250\text{K}$ and $3750 \pm 250\text{K}$ for the hot and cool component respectively, while the luminosity ratio ($L_{\text{warm}}/L_{\text{cool}}$) = 1.8. For both components we independently found the same reddening of $E(B - V) = 1.2 \pm 0.1$ mag. The fit together with the observations is shown in Fig. 5.

The relatively small luminosity difference between both stars suggests that *both* components are evolved, i.e. the M star is a giant or supergiant. A more detailed comparison of the ISO 2.4-5 μm spectrum with that of other M giants and supergiants indicates a supergiant nature of the spectrum (Van Winckel et al., in prep).

The flux from the central part of the ground-based 10 μm image is about 15 Jy. This is much larger than the flux expected from the stellar atmospheres of both stars in the system (3 Jy). This suggests that there is additional circumstellar material very close to the binary, probably hot dust. It is not clear whether this material was ejected at the same time as the dust and gas in the detached shell, or whether this represents a later phase of mass loss. The additional circumstellar material could also originate from the M-star in the system. Note that the flux of the second brightest blob, SW of the central peak, is still about 7 Jy, which is also enough to contain one or even both stars. However one should keep in mind that both stars show the same reddening, suggesting that they are located behind the same dusty material and that more clumps (e.g. SE, E and NNE of the central peak) are present.

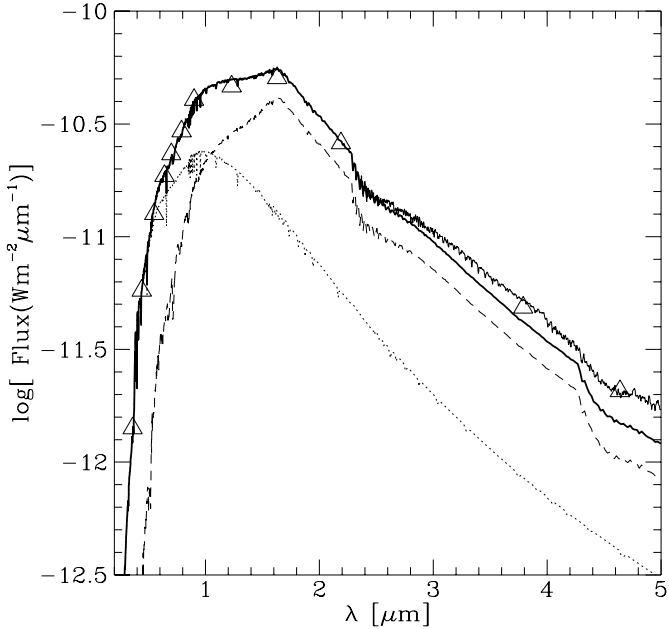


Fig. 5. The reddened ($E(B - V) = 1.2$) composite spectrum (thick line) of the hot star (dotted line) and the cool star (dashed line) compared with the broadband photometry (triangles) and the ISO-data (thin line). The error in the photometry is much smaller than the size of the triangles.

3.1. Interstellar and circumstellar extinction

The large reddening of AFGL 4106 is illustrated by the prominent diffuse interstellar bands (DIB's) in the optical spectrum of AFGL 4106. In Fig. 6 we display part of the

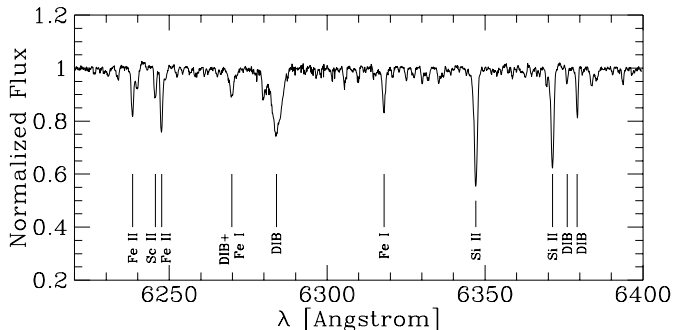


Fig. 6. High-resolution optical spectrum of AFGL 4106. The prominent interstellar DIB's are indicated together with the main photospheric atomic absorption lines. The spectrum has been corrected for the presence of telluric lines.

optical spectrum taken by van Winckel et al. (in prep.)

λ (\AA)	AFGL 4106 EW(\AA)	BD+36 $^{\circ}$ 1964 EW(\AA)	$W_{\lambda}/E(B-V)$
5849.78	72.	121.	48.
6196.19	76.	78.	61.
6325.10	33.		18.
6330.42	42.	16.	18.
6376.02	37.	28.	26.
6379.27	140.	176.	78.
6425.72	22.	25.	19.
6613.72	319.	316.	231.
6660.64	51.	57.	51.
6993.18	80.		116.
7224.18	252.		259.

Table 3. Equivalent width of a selection of DIB's in the optical spectrum of AFGL 4106 compared to the strength of same DIB's in BD+63 $^{\circ}$ 1964 (Ehrenfreund et al. 1997) and the DIB's-reddening relation of Jenniskens & Désert

corrected for telluric lines. The broad band at 6284 \AA , which is a blend of different components, is strong, but also the narrow DIB's at 6376 and 6379 \AA can easily be recognized. Since the carriers of the DIB's are associated with the carbon-rich component of the interstellar medium (ISM) and the circumstellar material around AFGL 4106 is oxygen-rich, the DIB's are likely to be purely from interstellar origin and can be used to estimate the interstellar component of the total reddening of AFGL 4106. The strength of the DIB's scales only roughly with the reddening ($E(B - V)$) (see Herbig 1995), therefore our quantisation of the interstellar reddening is only indicative.

We compared the strength of the DIB's in AFGL 4106 with the DIB strength in BD+63 $^{\circ}$ 1964 ($E(B - V) = 1.01$ mag., Spectral type B0II) (Ehrenfreund et al. 1997) and derived a second estimate of the reddening by using the equivalent width to reddening relation derived by Jenniskens & Désert (1994) from a detailed analysis of 4 reddened early-type stars. We limited ourselves to narrow DIB's without photospheric contamination since the broad DIB's in our spectrum are composite and the equivalent width determination most inaccurate. The equivalent width measurements are given in Table 3. One can see that the DIB's in AFGL 4106 and BD+63 $^{\circ}$ 1964 are very similar. We estimate the reddening using a linear least mean square analysis and found $E(B - V) = 1.07$ mag. by using the mean relation of Jenniskens & Désert and a similar value $E(B - V) = 0.94$ mag. by using BD+63 $^{\circ}$ 1964 as a standard. We conclude that the interstellar reddening towards AFGL 4106 is $E(B - V) = 1.0 \pm 0.2$ mag. This is in very good agreement with the value derived by van Loon et al. (in prep).

The case of AFGL 4106 offers a unique opportunity to measure the *internal extinction* within the circumstellar dust shell. This is because the star and the dust shell

are surrounded by a shell of ionized gas, detected in H α and the [N II] line. These emission lines were reported by García Lario et al. (1994), and subsequent imaging of the spatial extent of the emission lines by Van Loon et al. (in prep.) showed that the lines originate from a roughly spherical shell of gas on the periphery of the dust shell. The [N II] lines were found to be split, with the redshifted component systematically weaker than the blue peak. Van Loon et al. (in prep.) interpret this difference in intensity as a result of internal extinction in the dust shell, and assuming a reddening law which is the same for the interstellar as well as for the circumstellar dust, they found a circumstellar reddening towards the central star of $E(B - V) = 0.22 \pm 0.05$ mag. We conclude that sum of the DIB (interstellar) extinction of about $E(B - V) = 1$ mag. and the [N II] (circumstellar) extinction of about $E(B - V) = 0.2$ mag. agrees well with the derived total line-of-sight extinction of $E(B - V) = 1.2$ mag. based on the SED.

From the total spectrum one can derive the total flux, infrared excess and therefore another estimate of the interstellar and circumstellar absorption towards AFGL 4106. We define the infrared excess as the integrated flux under the energy distribution corrected for the stellar contribution. The distance to AFGL 4106 is not known, so we can only determine a distance dependent luminosity, which is roughly $10.8 \times 10^3 d^2 L_{\odot}$, with d the distance in kpc. The IR-excess contributes about 75% ($8.0 \times 10^3 d^2 L_{\odot}$) to the total luminosity. Which leaves $2.8 \times 10^3 d^2 L_{\odot}$ for the luminosity directly from the reddened photospheres of both stars. Assuming an $E(B - V)$ of 1.2 mag. for both stars, taken from the fit to the broad-band photometry, results in a dereddened luminosity of $\approx 7.4 \times 10^3 d^2 L_{\odot}$ for the hot component and $\approx 4 \times 10^3 d^2 L_{\odot}$ for the cool one. This implies a total “loss” of stellar energy by absorption and scattering of $\approx 8.6 \times 10^3 d^2 L_{\odot}/s$. This would imply that, assuming a spherical dust shell and assuming that all absorbed energy is re-radiated in the infrared, more than 90% of the extinction towards AFGL 4106 is circumstellar, and thus the contribution of the interstellar extinction would be negligible. This is not in agreement with the estimate of the interstellar extinction derived from the depth of the DIBs (see above). In Sect. 5.2 we will demonstrate that this discrepancy is resolved by the non standard extinction properties of the CSE.

4. The 5 – 195 μm part of the spectrum; The dust shell

At wavelengths longwards of about 5 μm thermal emission from the circumstellar dust starts to dominate the spectrum (see Fig. 2). Between 5 and 7.8 μm the spectrum is flat at a level of approximately 15 Jy. Around 7.8 μm a steep rise is found with a flattening around 12 μm . This prominent structure is caused by an increasing continuum together with the 10 μm amorphous silicate feature (Si-O

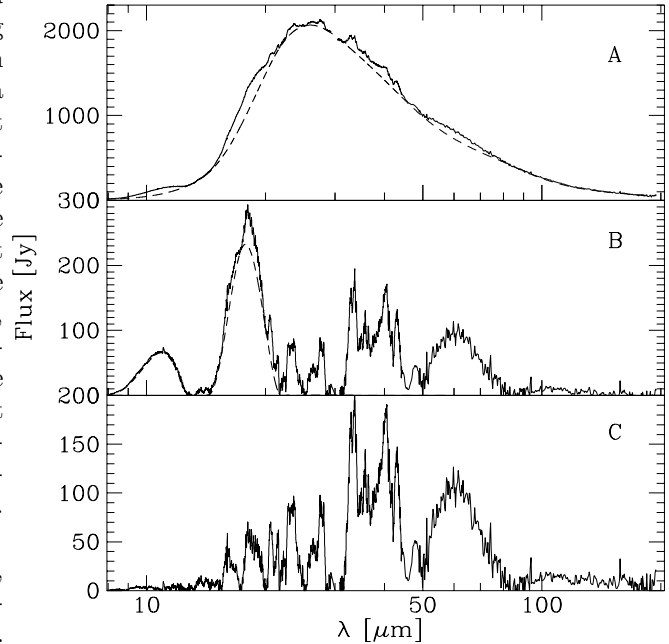


Fig. 7. The SWS and LWS spectrum of AFGL 4106 with the spline fit continuum. The result of the subtraction of the spline fit continuum (dashed line in A) is shown in graph B. The result of the removal of the broad silicate features (dashed line in B) is given in graph C.

stretching mode). At 13 μm the flux increases again, with at around 18 μm the second peak of the amorphous silicate feature (O-Si-O bending mode). The peak of the infrared excess is found around 25 μm . Superimposed on this continuum with the broad features are narrow features, especially in the SWS part of the spectrum. In most cases they can be attributed to crystalline silicates.

In contrast with the SWS spectrum with its sharp spectral features, the LWS spectrum of AFGL 4106 is very smooth. Emission lines are present in the on-source spectrum at 88.356 ([O III] line) and 157.741 μm ([C II] line). However, since they are also present in the background spectrum, they cancel out almost completely in the final spectrum. Although the warm component in the binary is not hot enough to produce the [O III]-line, the presence of the [O III]-line may not be surprising given the line of sight (Carina) and the projected vicinity of several very luminous hot stars, which emit enough ionizing radiation to produce the [O III]-line. We find no evidence for emission lines in the SWS and LWS infrared spectra from the ionized nebula surrounding AFGL 4106 (detected at optical wavelengths), which should be within the ISO beam. Clearly the dust continuum swamps any line emission from that region.

4.1. The continuum subtraction of the SWS and LWS spectra

In order to show the presence of the spectral features more clearly, we have subtracted a continuum by fitting a spline curve to the spectrum. Note that the spline fit continuum has no physical meaning and is only used to enhance the sharp solid state features on top of the spectrum. The continuum subtracted spectrum is shown in Fig. 7 panel B. The amorphous silicate features dominate the continuum subtracted spectrum below 20 μm . In order to show the narrow bands more clearly, we have created a second continuum subtracted spectrum, where we have excluded the broad amorphous silicate bands (see the dashed line in Fig. 7 panel B and the result in panel C). We find a wealth of solid state structures, which we show in more detail in Fig. 8. Some residual fringing is still visible at 18-20 μm .

Since the solid state bands have a wide range in width and strength, and often blend, we decided to measure the band strength with respect to a *local continuum*. We used a second order polynomial fit to define a local continuum in the final spectrum (i.e. not the continuum subtracted spectrum shown in Fig. 7 and 8), and fitted Gaussians to the emission bands with respect to this local continuum. The very broad amorphous silicate bands could not be fitted with a single Gaussian, and we give the FWHM directly measured from the spectrum. The results of the Gauss-fits can be found in Table 4. Due to our continuum subtraction method, it is likely that very broad features have been included in the continuum and therefore are not visible in the continuum subtracted spectrum.

In the following sub-sections, we briefly describe the continuum subtracted spectrum.

4.1.1. The 10-20 μm region

The Si-O stretching and O-Si-O bending mode vibrations of the amorphous silicates dominate the 10 - 20 μm part of the spectrum. We note that the peak wavelength of the Si-O stretch is significantly red-shifted compared to the bump found in most O-rich (post-)AGB stars (Monnier et al. 1998) and the ISM. However, Little-Marenin and Little (1988, 1990) find in LRS spectra an emission feature which peaks at a similar position in most S-, several MS- and some (5%) M-type stars. On top of the amorphous silicates are narrow emission features. Careful inspection of the raw data suggests that there are three instrumental artifacts at 11.07 and probably 13.6 and 14.2 μm , but the other features at 16.1, 16.8, 18.1 and 19.2 μm are of circumstellar dust origin. The identification of most of these narrow peaks can be found in Table 4 and Sect. 4.2.

4.1.2. The 20-29.5 μm region

The spectral region between 20 and 29.5 μm is shown in Fig. 8 and is characterized by a wealth of emission fea-

tures with a range of FWHM; we find narrow features (FWHM/ $\lambda < 0.03$) at 20.6, 21.5, 22.9 and 24.1 μm , and broader features (FWHM/ $\lambda > 0.03$) at 23.6, 26.2, and 27.8 μm . The sharp descent at the long wavelength side of the 21.5 μm feature and rise at the short wavelength side of the 22.9 μm feature are probably caused by an imperfect responsivity calibration.

4.1.3. The 29.5-45 μm region

As stated in Sect. 2.1.1 we excluded 29.5 to 31 μm from the final spectrum, but we can say that we did not detect narrow emission bands in this wavelength range. The spectral region from 29.5 to 45 μm is dominated by a broad structure from about 31 to 44 μm , on top of which emission features are present, see also Fig. 8. We find broad features at 33.6, 40.4 and 43.1 μm and narrow features at 32.8, 34.0, 35.8, 36.5 and 41.1 μm . Waters et al. (1996) find a weak plateau from 32 to 37 μm in the spectrum of several oxygen rich dust shells. This plateau is also visible in AFGL 4106, although it is weak and blends with the broad unidentified structure from 31 to 44 μm . There is also evidence for sub-structure in the 32-33 μm region, suggesting another weak band that contributes. This weak band at 32.0 μm is also seen in the SWS spectrum of NGC 6302 (Lim et al., in prep.) and in that of HD44179 (the ‘‘Red Rectangle’’, Waters et al. 1998).

4.1.4. The 45-195 μm region, LWS

At longer wavelengths, the spectrum is smooth. We find a narrow band at 47.8 μm , and a broad emission centered at 61 μm (probably due to H₂O-ice). Also, the [C II]-line at 157 μm is present; this is likely due to imperfect cancellation of the on-source and off-source caused by the gradient found in the background (see also the remarks in Sect. 2.1.3). For the moment, we ignore the [C II]-line emission.

4.2. Identifications

4.2.1. Amorphous silicates

The broad emission features around 10 and 18 μm are attributed to amorphous silicates. We have derived a rough estimate of the temperature of 140 K for the amorphous dust component using the amorphous olivine optical constants published by Dorschner et al. (1995) (see also Fig. 9). Such a temperature estimate should be used with caution, since the features are on top of a steep continuum and contribution from other species (e.g. FeO) can affect the 10 over 18 μm band strength ratio. A similar temperature was found by fitting the shape of the dust spectrum with a dust emissivity $Q(\lambda) \propto \lambda^{-1}$. This simple procedure even fits the long wavelength part very well but is significantly too low from 15 to 50 μm .

λ μm	F_{band} 10^{-14} Wm^{-2}	FWHM μm	FWHM/ λ	$I_{\text{peak}}/I_{\text{cont}}$	Identification	Comments
10.8	4×10^2	2.5	0.23	1.8	amorph. silicate	
16.1	40.	.7	0.043	1.06	cryst. forsterite	on the slope of the 17.6 μm feature and measured together with the 16.8 μm peak
16.8	15.	.6	0.036	1.03	unidentified	on the slope of the 17.6 μm feature and measured together with the 16.1 μm peak
17.6	5×10^2	3.	0.17	1.2	amorph. silicate	
18.1	75.	1.0	0.055	1.07	cryst. enstatite	on the slope of the 17.6 μm feature and measured together with the 19.2 μm peak
19.2	50.	1.0	0.052	1.045	cryst. enstatite and cryst. forsterite	on the slope of the 17.6 μm feature and measured together with the 18.1 μm peak
20.6	20.	0.48	0.023	1.035	cryst. enstatite ?	
21.5	7.3	0.25	0.012	1.024	cryst. enstatite and cryst. forsterite?	Sharp edge caused by responsivity
22.9	25.	0.5	0.021	1.04	unidentified	measured together with the 23.6 μm peak Sharp edge caused by responsivity
23.6	30.	0.7	0.030	1.04	cryst. forsterite	measured together with the 22.9 μm peak
24.1	1.8	0.16	0.0066	1.009	unidentified	On the slope of the 23.6 micron feature
24.5	4.1	0.33	0.013	1.011	cryst. enstatite?	On the slope of the 23.6 micron feature
26.2	16.	1.05	0.040	1.02	cryst. forsterite	
27.8	44.	1.15	0.041	1.05	cryst. forsterite and cryst. enstatite	
32.8	20.	.6	0.018	1.07	cryst. enstatite	measured together with the 33.6 μm peak see remarks in text
33.6	40.	1.0	0.030	1.08	cryst. forsterite	measured together with the 32.8 μm peak
34.0	.96	.12	0.0035	1.016	cryst. enstatite ?	on the slope of the 33.6 μm peak
35.8	5.5	.54	0.015	1.03	cryst. enstatite	
36.5	2.4	.28	0.0077	1.02	cryst. forsterite	
40.4	13.	1.1	0.027	1.05	cryst. enstatite	
41.1	1.1	.17	0.0041	1.02	unidentified	on the slope of the 40.4 μm peak
43.1	17.	1.2	0.028	1.07	cryst. enstatite and cryst. H ₂ O	
47.8	9.	1.9	0.040	1.036	unidentified	
61	68.	20.	0.33	1.05	cryst. H ₂ O	
Spurious features						
11.07	1.98	0.082	0.0074	1.05		instrumental artifact
13.6	10.	.5	0.037	1.04		measured together with the 14.2 μm peak instrumental artifact?
14.2	6.5	.4	0.028	1.05		measured together with the 13.6 μm peak instrumental artifact?

Table 4. The characteristics of the dust features in the spectrum of AFGL 4106

4.2.2. Crystalline olivines and pyroxenes

We use the laboratory transmission spectra of crystalline silicates as measured by Jäger et al. (1998) and Koike & Shibai (1998) to identify the rich solid state spectrum. The identifications are based on the match between the laboratory peak positions and observed peak positions for the minerals of the olivine ($\text{Mg}_{2x}\text{Fe}_{(2-2x)}\text{SiO}_4$) and pyroxene ($\text{Mg}_x\text{Fe}_{(1-x)}\text{SiO}_3$) family. We find a very good match between the most (but not all) broad emission bands and the laboratory data for the pure Mg end member of the crystalline olivine solution serie, i.e. forsterite (Mg_2SiO_4). Similarly, we can identify most narrow emission bands with the pure Mg end member of the crystalline pyroxene solution serie, i.e. enstatite (MgSiO_3). Enstatite comes in

two crystal structures, ortho- and clino-enstatite. However, apart from the 32.8 μm peak which is only found in ortho-enstatite (Koike & Shibai 1998) and blends with the 33.6 μm forsterite peak, the main strong peaks of clino- and ortho-enstatite are located at about the same position. For this reason we were not able to distinguish between these two forms in Table 4.

Apart from the wavelength of the bands, it is also important to consider the relative strength of the emission bands in the identification process, since it gives a rough estimate of the temperature. To estimate the temperature we compared the continuum subtracted spectrum of AFGL 4106, with the continuum subtracted spectrum of forsterite (and enstatite and diopside in Fig. 10). The continuum subtraction has been performed in the same way

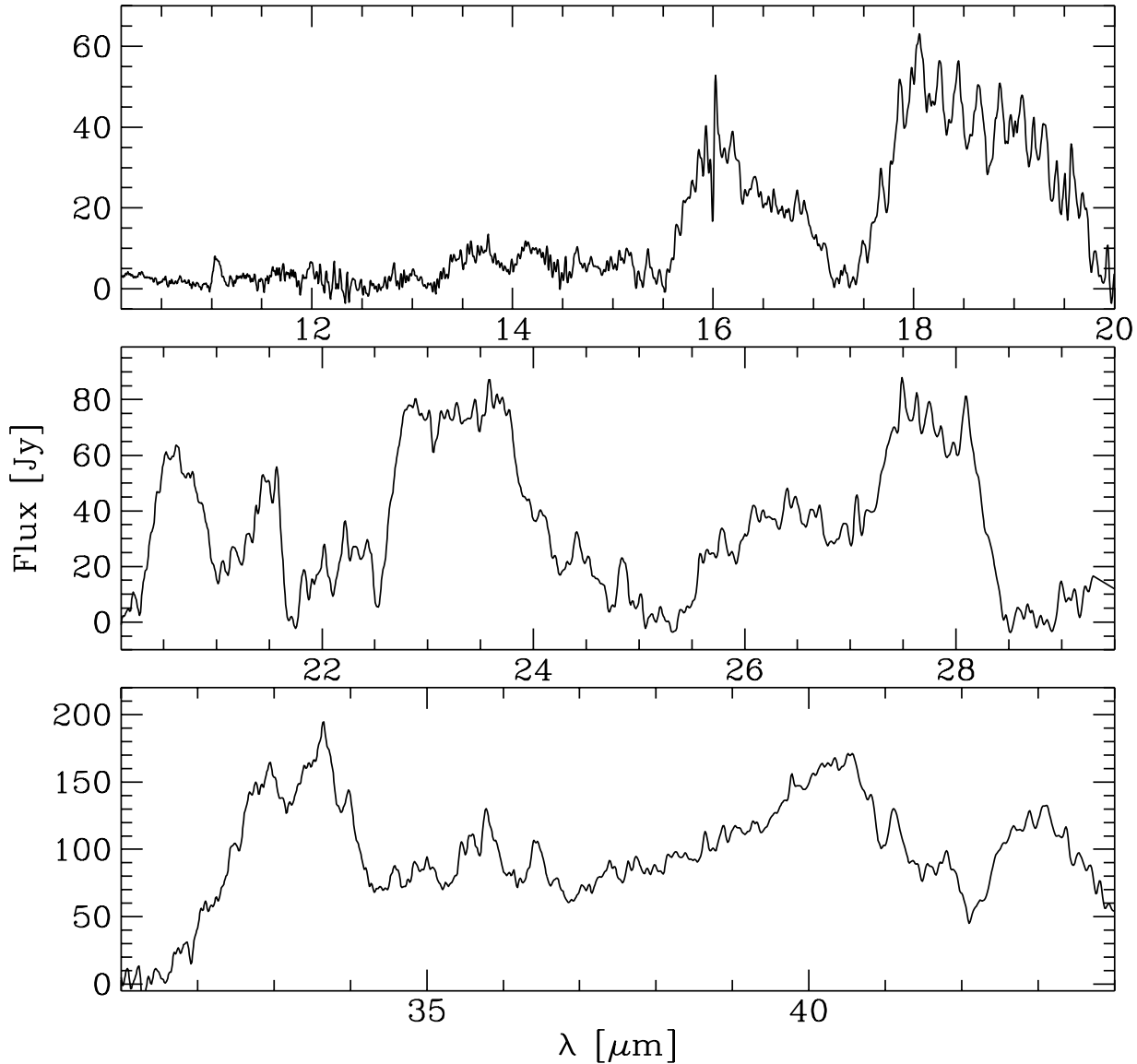


Fig. 8. The 10 to 44 μm region of the continuum subtracted spectrum enlarged. Note the richness of solid state features.

as it was done for AFGL 4106 (i.e. a smooth spline fit curve without obvious kinks) after multiplying the emissivity of the different dust species with blackbodies of the given temperatures. Since the peak of the features are at same wavelength for the two temperatures, which had quite different continua, it shows that this continuum subtraction does not shift the peaks. For forsterite we show in Fig. 9 the best fit to the continuum subtracted spectrum of AFGL 4106, assuming that the forsterite grains have a sin-

gle temperature. The best fit temperature is about 80 K. We stress that these temperature estimates are only approximate; a full treatment of the radiative transfer is discussed in Sect. 5. The temperature of the amorphous dust is significantly higher than that of the crystalline component: a temperature of 140 K for the forsterite would have resulted in significant emission in the 11.2 μm band, which is not observed. We conclude that amorphous and crystalline dust are not thermally coupled and that they

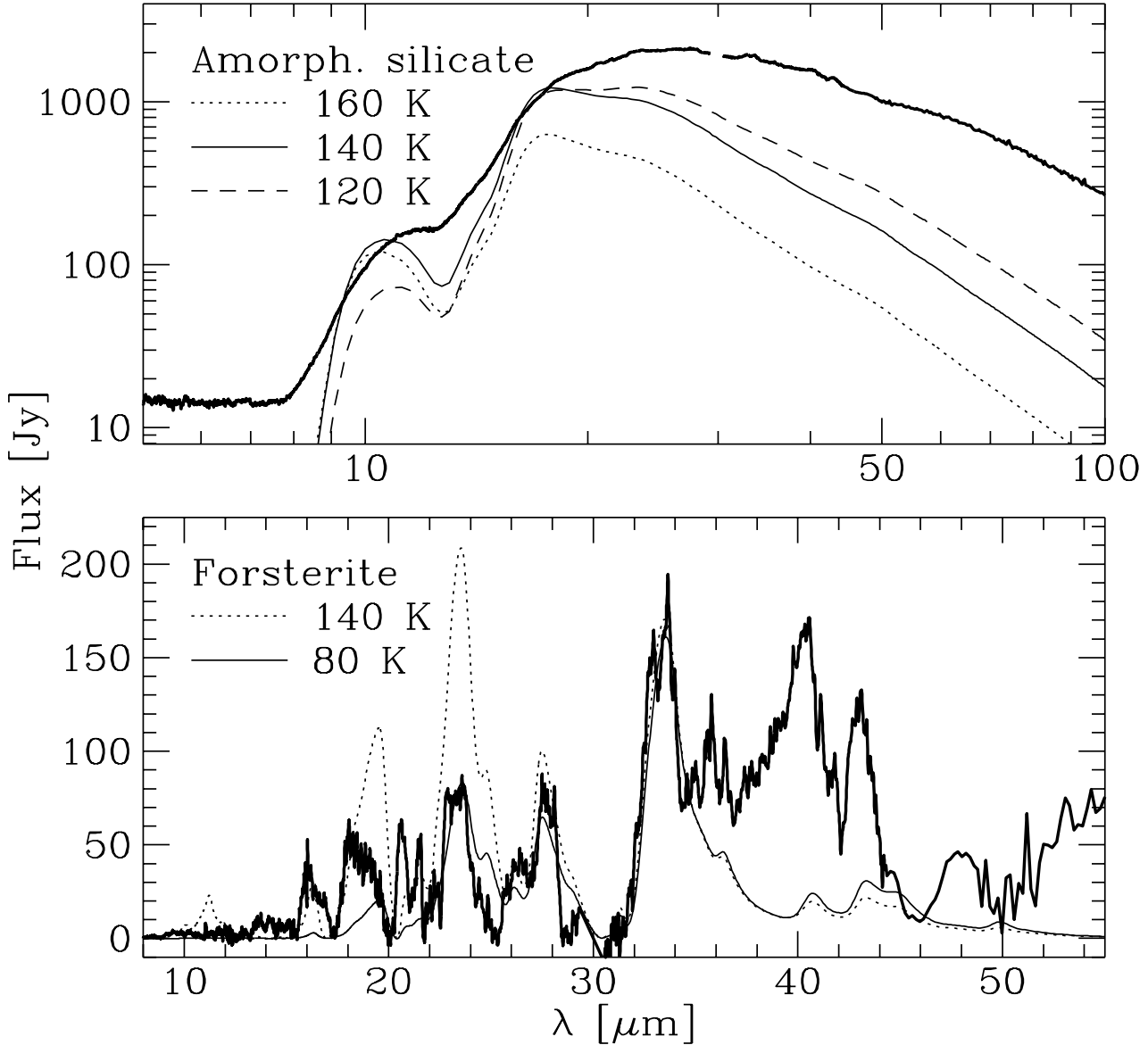


Fig. 9. The emission spectrum of a 120, 140 and 160 K grain of amorphous olivine ($\text{Mg}_{0.8}\text{Fe}_{1.2}\text{SiO}_4$, Dorschner et al. 1995) compared with the spectrum of AFGL 4106 (upper panel), and the continuum subtracted emission spectrum of a 80 and 140 K crystalline forsterite (Jäger et al. 1998) grain compared with the continuum subtracted spectrum of AFGL 4106 (lower panel).

either have quite different optical properties, or are spatially distinct.

Unfortunately, the situation is rather disappointing for the pyroxenes. The observed band strengths of AFGL 4106 poorly match the band strengths seen in the laboratory data published by Jäger et al. (1998). Therefore we cannot derive a reliable characteristic temperature for the py-

roxenes, based on these laboratory data. We have also compared the band strengths of pyroxenes measured by Koike & Shibai (1998) to our AFGL 4106 data which gives a slight improvement of the match, especially in the $32.8 \mu\text{m}$ range (see Fig. 10). A temperature of 80 K gives again a reasonable fit to the data. The difference between these two laboratory spectra might be caused by slight dif-

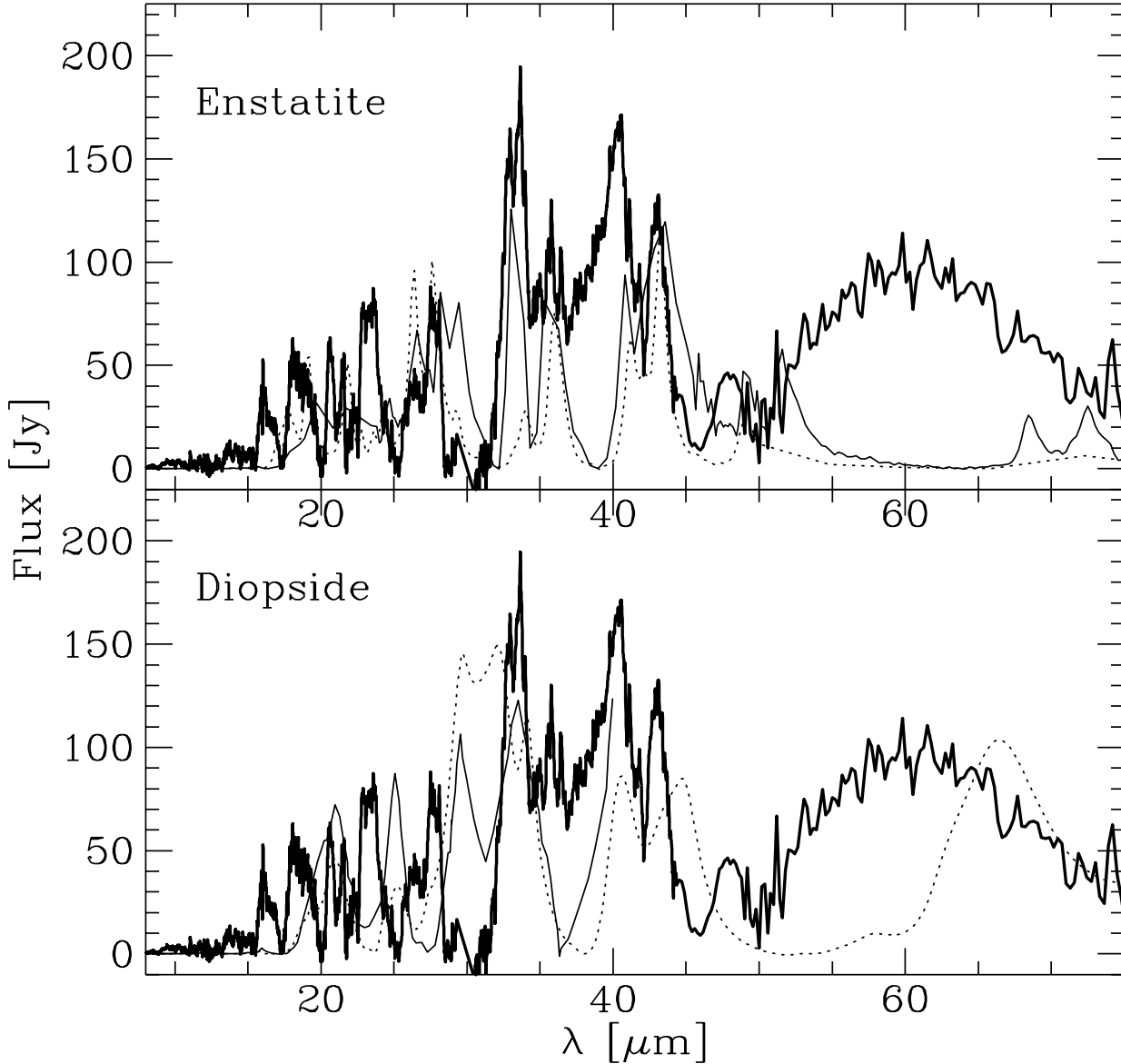


Fig. 10. Upper panel: The continuum subtracted emission spectrum of a 80 K crystalline ortho-enstatite grain from Koike & Shibai (1998) (thin solid line) and from Jäger et al. 1998 (dashed line) compared with the continuum subtracted spectrum of AFGL 4106 (thick solid line). Lower panel: The continuum subtracted emission spectrum of a 80 K crystalline diopside grain from Koike & Shibai (1998) (thin solid line) and a diopside measured by Jäger (private communication) compared with the continuum subtracted spectrum of AFGL 4106 (thick solid line).

ferences in the chemical composition. The natural ortho-enstatite sample of Jäger et al (1998) is not the pure Mg end member of the crystalline pyroxene solution series but contains 2.1 mass % FeO, while the data of Koike & Shibai (1998) is of a synthetic sample of enstatite with some small impurities from LiO_2 , MoO_3 and V_2O_5 . Whether this dif-

ference at $32.8 \mu\text{m}$ is due to the small amount of FeO, which has influence on the peak over continuum ratio (see e.g. Fig. 2 and Fig. 3 of Jäger et al. (1998)), or due to the metaloxides found in the ortho-enstatite of Koike & Shibai (1998) is not known yet, but we will tentatively identify it with enstatite. For both the olivines and the pyroxenes

the observed FWHM of the bands are significantly smaller than those measured in laboratory spectra. It is interesting to note that both in the laboratory spectra and in our ISO data the olivine bands are broader than the pyroxene bands.

The main component for the plateau from 32 to 37 μm is unidentified yet. Its appearance and shape are influenced by the forsterite bands at 33.6 and 36.5 μm and the enstatite band(s) at 35.8 (and 32.8) μm , which makes it difficult to extract the unblended shape of this feature and therefore its identification.

4.2.3. Diopside

A third silicate that was checked for its presence is diopside (CaMgSiO_3). In Fig. 10 we show the comparison of diopside with the spectrum of AFGL 4106. Although the two datasets (Koike & Shibai, 1998; Jäger, private communication) used for comparison show some differences, probably due to a somewhat different chemical composition, both datasets predict prominent emission at 21 and 25 μm , which is not observed in our spectrum. We conclude that the presence of diopside cannot be confirmed at present.

4.2.4. Aluminum rich dust

In Sect. 5.2 we will demonstrate that corundum ($\alpha\text{-Al}_2\text{O}_3$) is present in the dust shell of AFGL 4106. According to the condensation scheme published by Tielens (1990) corundum can transform into melilite ($\text{Ca}_2\text{Al}_2\text{SiO}_7$). It is not known by the authors if melilite will form below or above the glass temperature. Since we only have optical data for amorphous melilite (Mutschke et al. 1998) we will concentrate on this. Amorphous melilite shows broad features at 10, 15, 19 and 34 μm . Because of the amorphous structure the features are very broad and difficult to identify in the spectrum. However the very broad (several μm) feature at 34 μm might be a good candidate for the broad structure from about 31 to 44 μm found in our ISO-spectrum.

4.2.5. Water ice

We have identified the feature at 61 μm , hereafter referred to as the 60 μm feature, with crystalline H_2O ice. Omont et al. (1990) identified a similar feature observed with KAO in IRAS 09371+1212 (Frosty Leo) with crystalline H_2O ice, while Barlow (1998) reports the presence of 60 μm emission in several dusty circumstellar shells. Laboratory data published by Bertie et al. (1969) show that crystalline H_2O ice has two strong bands, one at about 43 μm , the other at roughly 61 μm . In the SWS spectrum we already found a broad and strong emission feature at 43.1 μm , which is probably a blend of crystalline enstatite and crystalline H_2O -ice. The fact that a 60 μm feature is present strengthens the crystalline H_2O -ice identification.

Assuming that the 43.1 μm feature is a blend of different

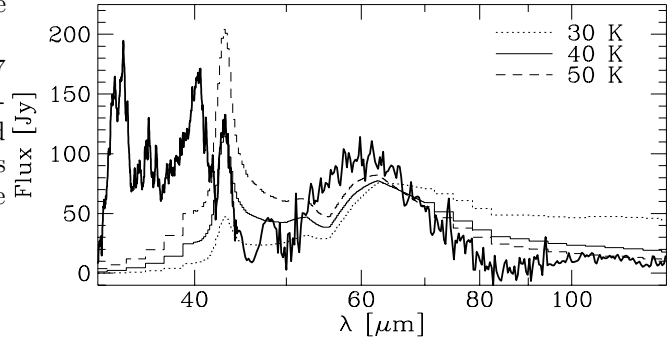


Fig. 11. The emission spectrum of a 30, 40 and 50 K crystalline H_2O -ice grain (Bertie et al. 1969) compared with the continuum subtracted spectrum of AFGL 4106.

features, including crystalline H_2O -ice, we have derived an upper limit of the temperature of only 40 K. This is again much lower than the amorphous silicate temperature but also significantly lower than the crystalline silicate temperature. It cannot be excluded that the 60 μm feature is in fact a blend. We note that the laboratory spectra of clino-enstatite (Koike & Shibai 1998) show a weak 60 μm bump. This would result in a higher temperature for the crystalline H_2O ice. Still it points to another grain population which is not thermally coupled with the others.

4.2.6. Iron oxides

The identification of Mg-rich and Fe-poor crystalline silicates in non-negligible abundances suggests that some Fe may be present in the form of simple oxides. For spherical FeO grains the most important infrared feature longwards of 10 micron is a relatively sharp feature at 20 μm , which is not present in our spectrum. However FeO is very sensitive to shape effects (Henning & Mutschke 1997). In the case of a continuous distribution of ellipsoids (CDE, Bohren & Huffman 1983) the 20 μm peak broadens significantly, the FWHM becomes roughly 8 μm , and also shifts to 24 μm . This feature is temperature dependent (Henning & Mutschke 1997) but only in absolute strength and not in wavelength. The broad feature is present in our total spectrum, but hidden in the “continuum” in the continuum subtracted spectrum. If FeO is present it is possible that Fe_2O_3 (hematite) and Fe_3O_4 (magnetite) are also present. We have compared laboratory spectra of Fe_2O_3 (Steyer 1974) to our observations. This oxide has strong bands in the 15-45 μm region, that are sensitive to grain shape effects. We were unable to find reasonable fits to the observed spectra for spherical and for a CDE mixture. We conclude that Fe_2O_3 is not very abundant or absent in AFGL 4106.

Fe_3O_4 (magnetite) is quite featureless, except for a strong resonance at $17.5 \mu\text{m}$ and a weak one at $26.5 \mu\text{m}$. These features are temperature dependent, not only in strength but also in shape and position and they have the tendency to shift to shorter wavelengths when the temperature decreases. At 150 K the $26.5 \mu\text{m}$ feature is split in two features at 25.4 and $26.7 \mu\text{m}$, while the $17.5 \mu\text{m}$ feature shifts to $17.1 \mu\text{m}$. Since we do not see strong features in the wavelength range from 17.0 to $17.5 \mu\text{m}$ hardly any magnetite seems present.

4.2.7. Unidentified features

We find a narrow emission band at $47.8 \mu\text{m}$; although the wavelength of this feature is close to a spectral structure in the responsivity curve of LWS and a instrumental artifact can therefore not be excluded, quite convincing evidence for its presence was given by Barlow et al. (1998) in the spectrum of several oxygen-rich sources with crystalline silicates at shorter wavelengths. According to the optical constants of Steyer (1974), almandine ($\text{Fe}_3\text{Al}_2(\text{SiO}_4)_3$) peaks at 48 and $60 \mu\text{m}$. However, other peaks of almandine, e.g. at 42 and $31.5 \mu\text{m}$, are not observed. Therefore we exclude this possibility. We have not found a convincing identification for this band, but given its width it is likely caused by a crystalline silicate.

Several other peaks remain, which are not yet firmly identified (e.g. 16.8 , 20.6 , 22.9 and $24.1 \mu\text{m}$). It is therefore (very) likely that more dust components are present.

5. Radiative transfer modelling

In this section we model the observed SED of AFGL 4106 with a one-dimensional radiative transfer code (MODUST, Bouwman & Waters, 1998; Bouwman et al. in prep.; de Koter et al., in prep.). From the structure seen in the N-band images it is clear that this approach is not entirely correct. Since AFGL 4106 is only marginally extended for ISO, we assume that diffraction losses can be neglected.

5.1. Dust species

We have tried to collect optical constants of the dust species, that are identified in the previous section. Unfortunately, in many cases the optical constants are given only for a limited wavelength range, and we had to combine data sets from different authors or extrapolate to cover the full wavelength range required for our modelling. The data sets used for the modelling can be found in Table 5.

We assume spherical grains and a power-law size distribution and we use Mie theory to calculate the optical properties of the grain population. This approach allows us to calculate the emission for arbitrarily large grains. As

we will show below, large grains are abundant in the shell of AFGL 4106.

Since we identified both crystalline olivines as well as crystalline pyroxenes in our spectrum, it is likely that also both components are present in the amorphous state. For the amorphous olivines we applied the optical constants derived by Dorschner et al. (1995). Unfortunately they only published optical constants for two different Fe/Mg ratios ($\text{Mg}_{0.8}\text{Fe}_{1.2}\text{SiO}_4$ and $\text{Mg}_{1.0}\text{Fe}_{1.0}\text{SiO}_4$). So, although the more Fe-rich olivine fits the data slightly better, it only gives a rough estimate of the Fe over Mg ratio for the amorphous olivines.

Dorschner et al. (1995) also derived optical constants for amorphous pyroxenes ranging from MgSiO_3 to $\text{Mg}_{0.4}\text{Fe}_{0.6}\text{SiO}_3$. Amorphous pyroxenes with the same percentage of Fe as the amorphous olivines produce a peak around $21 \mu\text{m}$, which is not seen in our ISO-spectrum. Only when the Fe content drops below 0.2 (i.e. Mg higher than 0.8), the peak vanishes. For Mg-rich amorphous pyroxenes with a Mg content above 0.8 only two sets of optical constants are available ($x=1$ and 0.95 in $\text{Mg}_x\text{Fe}_{(1-x)}\text{SiO}_3$). Since the emissivity of the Fe-poor pyroxenes is very dependent on the Fe content, it is difficult to give a reliable estimate of the contribution of the amorphous Fe-poor pyroxenes based on these 2 sets only. Amorphous pyroxenes, if present at all, will only marginally contribute to the IR-excess, due to their lower Fe content compared with the amorphous olivines, unless they have an efficient thermal coupling with Fe-containing dust, due to an aggregate or a core mantle structure. Since we have already found indications for separate grain populations, see e.g. the temperature differences found for the amorphous and crystalline olivines, we assume that these two component grains do not exist and only the amorphous Fe-rich olivines are present.

Crystalline forsterite has 3 different crystallographic axes. We found two studies of the optical constants of the 3 axes, one by Servoin & Piriou (1973) who used a synthetic sample and one by Steyer (1974), who used a natural sample. Both data sets do not cover the whole wavelength range. Although both sets of optical constants should describe the same material there were quite some differences. The Steyer (1974) optical constants were not able to reproduce the correct wavelengths of the 23.5 and $33.5 \mu\text{m}$ bands, found in laboratory transmission measurements (Koike et al. 1993; Jäger et al. 1998), even when shape effects or core mantle structures were taken into account. The Servoin & Piriou (1973) data set predicts for spherical grains peaks at shorter wavelengths than observed. A CDE mixture produces peaks that are at slightly longer wavelengths than observed. It is likely that a somewhat modified CDE mixture will give a good match. The difference between the Steyer and Servoin & Piriou data may be related to the origin of the samples, i.e. respectively natural and synthetic. Since Servoin and Piriou only have data longwards of $5 \mu\text{m}$ we extended the data set to

Dust species	Chemical formula	λ (μm)	reference
olivine (amorphous)	$\text{Mg}_{0.8}\text{Fe}_{1.2}\text{SiO}_4$	0.1 – 0.2	extrapolated
		0.2 – 500	Dorschner et al. (1995)
		500 – 1500	extrapolated
forsterite (crystalline) (all 3-axes)	Mg_2SiO_4	0.1 – 5.0	Scott & Duley (1996)
		5.0 – 125	Servoin & Piriou (1973)
		125 – 1500	extrapolated
water ice	H_2O	0.1 – 1.25	extrapolated
		1.25 – 333	Bertie et al. (1969)
		333 – 1500	extrapolated
iron-oxide	FeO	0.1 – 0.2	extrapolated
		0.2 – 500	Henning et al. (1995)
		500 – 1500	extrapolated
corundum	$\alpha\text{-Al}_2\text{O}_3$	0.1 – 0.5	extrapolated
		0.5 – 400	Koike et al. (1995)
		400 – 1500	extrapolated

Table 5. The dust species used for the radiative transfer modelling

the shorter wavelengths using amorphous forsterite data as published by Scott & Duley (1996), assuming that the absorption properties of the amorphous and crystalline grains do not differ much in this part of the spectrum. For a fair determination of the abundance of the crystalline forsterite we will apply Mie theory, since we use the spherical shape also for the other dust species. However for the best fit we apply CDE, since this fits the position of the peaks much better. In this case the abundance is decreased with 25% because of the influence of size and shape effects on the peak to continuum ratio of crystalline forsterite.

To our knowledge no optical constants are available for the three different crystallographic axes of the pure Mg-end member of the crystalline pyroxene solid solution serie, enstatite (MgSiO_3). Jäger et al. (1998) have measured ortho-enstatite with a small amount of Fe ($\text{Mg}_{0.96}\text{Fe}_{0.04}\text{SiO}_3$). Given the problems mentioned in Sect. 4.2.2 it is clear that we cannot reproduce all the peaks with the desired strength for this set of optical constants, e.g. the $32.8 \mu\text{m}$ peak. Therefore we decided not to include enstatite in our model fit. We will derive the enstatite abundance in a different way (see Sect. 5.2).

An interesting point is how to combine the different grain components in model calculations. From an observational point of view, there appear to be several separate grain components: the large temperature difference between the amorphous and crystalline grains suggest that these components are not in thermal contact, which, assuming that they are co-spatial, implies that they should be treated as two independent grain populations in the radiative transfer. The situation is less clear for the different crystalline silicates. They may very well be incorporated in the same grain, and this can change the optical properties of the material significantly. We have tried to produce a forsterite-enstatite-aggregate grain theoretically with the Bruggeman (1935) method, and although the results are promising we will not use these results since no good op-

tical constants for the pure enstatite are available at the moment. For forsterite, with its three different crystallographic axes, we assumed an equal distribution of the orientation axes. This has been achieved by adopting 3 different grain populations, one for each axis. The number density, and thus the mass, of each population is one third of the total number density (mass) of the material.

Our code is not well suited for large, non-spherical grains. Therefore for FeO we use instead of Mie a CDE shape distribution, which is not strictly correct for the size distribution we expect. Since shape effects also change the emissivity of FeO, the abundance of FeO derived from our model fit should be used with great caution.

We have not included melilite, because optical constants with a sufficient large ($0.1\text{-}100 \mu\text{m}$) wavelength coverage were not available.

The final point of caution is the fact that we used blackbodies to represent the stellar continua. This will influence the result especially in the part where absorption from molecules dominates the stellar photosphere, but not for longer wavelengths where the dust emission dominates. A more detailed fit of the stellar photospheres will be presented by van Winckel et al. (in prep.).

5.2. The best fit model parameters

Our best fit to the SED can be seen in Fig. 12. The model parameters of the shell are given in Table 6, together with an estimate of their errors. Starting estimates for the inner and outer radius of the dust shell were derived from the TIMMI image, assuming a distance to AFGL 4106 of 3.3 kpc. This value will be discussed in Sect. 6.1. The dust shell is optically thin at most wavelengths. This implies that the inner and outer radius of the dust shell depend linearly on the distance, as does the duration of the mass-loss burst. The total mass in the shell scales roughly with the square of the distance, therefore the mass loss rate will

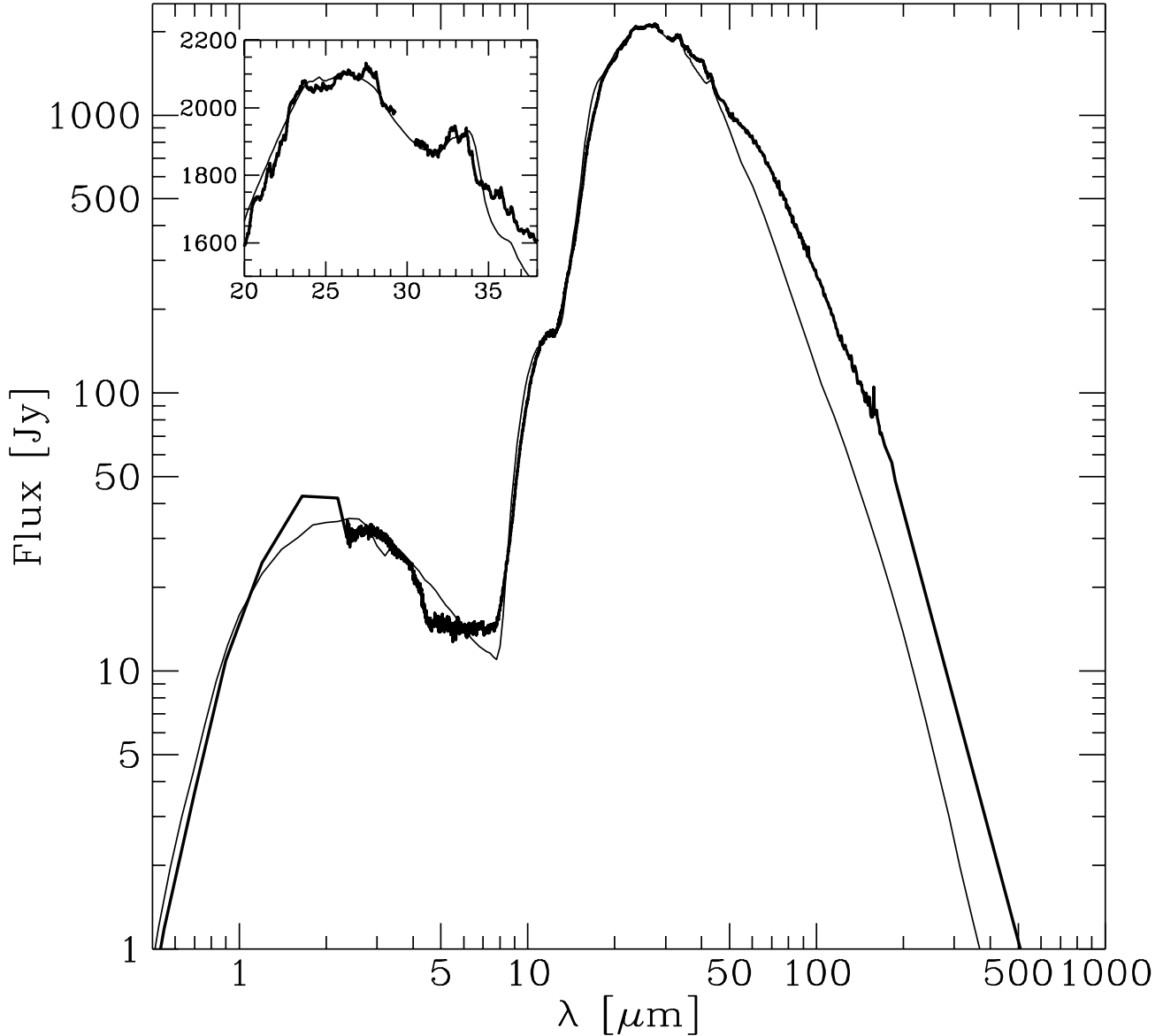


Fig. 12. The SED of AFGL 4106 (thick line) and our best model fit (thin line) The input values are those from Table 7, with the exception that enstatite was not put in and for forsterite and FeO we applied CDE instead of Mie.

also scale linearly while the density at the inner radius is inversely proportional to the distance.

In Table 7 the dust parameters used in the model are given. To minimize the number of free parameters, we have assumed that all grain-species have the same size distribution. The typical errors in the grain size are 25%. In all models we have assumed a size distribution $N(a) \propto a^{-3.5}$ (Mathis et al. 1977).

Apart from the uncertainty of the enstatite mass fraction, which influences the whole scheme, the errors in the mass fractions differ between the materials. For FeO the error is difficult to determine since the shape distribution largely influences the outcome, an order of magnitude cannot be excluded. The mass fraction of the amorphous olivines is accurate to a few percent of the total mass. However the chemical Fe:Mg ratio is not well determined in the amorphous olivines, a change of 10% in

Stellar properties			
$L_{\text{hot star}}$	1.3×10^5		L_{\odot}
$T_{\text{hot star}}$	7250		K
$L_{\text{cool star}}$	7.4×10^4		L_{\odot}
$T_{\text{cool star}}$	3750		K
Shell properties			
Inner radius	4.2	$\pm 1.0 \times 10^{16}$	cm
Outer radius	4.1	$\pm 1.0 \times 10^{17}$	cm
ρ at the inner radius	1.2	$\pm 0.2 \times 10^{-18}$	g/cm^3
exp in $\rho(R) = C \times R^{\text{exp}}$	-2.2	± 0.15	
M_{dust}	3.9	$\pm 1.0 \times 10^{-2}$	M_{\odot}
$\langle M \rangle$	9.	$\pm 2. \times 10^{-4}$	M_{\odot}/yr

Table 6. The fixed stellar input parameters together with the Model parameters for the best fit, assuming a distance of 3.3 kpc. The errors for the shell parameters are internal model errors.

Dust properties	
Grain size (μm)	0.4 - 6.0
Mass fraction of crystalline forsterite (Mg_2SiO_4)	4%
Mass fraction of crystalline enstatite (MgSiO_3)	4-11%
Mass fraction of crystalline water ice (H_2O)	5%
Mass fraction of crystalline corundum ($\alpha\text{-Al}_2\text{O}_3$)	17-15%
Mass fraction of amorphous olivine ($\text{Mg}_{0.8}\text{Fe}_{1.2}\text{SiO}_4$)	70-65%
Mass fraction of ironoxide (FeO)	< 1%

Table 7. The dust properties as derived from the radiative transfer model fitting. The ranges in the mass fractions come from the uncertainty about the enstatite to forsterite ratio.

this ratio will only marginally influence the spectrum. The crystalline forsterite abundance is mainly based on the strength of the 23.6 and 33.6 micron peak and has an error of about 1% of the total mass. The abundance of enstatite is hard to determine since no optical constants were available for this material. So, we used an alternative way to determine the enstatite to forsterite ratio. From transmission measurements of enstatite and forsterite one may determine the wavelength dependent extinction coefficients. The 33.6 μm peak is caused by forsterite and the 32.8 μm peak by ortho-enstatite. So the peak-strength ratio of these two features is indicative for the abundance ratio. Since the peak wavelengths of these two features are very close, temperature effects do not influence the results. If we use the transmission spectra published by Koike & Shibai, we find a ratio of enstatite to forsterite of 3. However, transmission spectra of forsterite published by Jäger et al. (1998) give a peak strength of the 33.6 μm feature which is 3 times smaller than that of Koike & Shibai (1998), from which a ratio of enstatite to forsterite of 1 follows. We conclude that, given the large spread in laboratory data published so far, we find an abundance ratio of enstatite to forsterite between 1 and 3. It would

be interesting to compare this value with the olivine to pyroxene ratio seen for the amorphous silicates. However, because of reasons given in Sect. 5.1 this is not possible at the moment.

Since we were not able to reproduce (in a single dust shell) the low temperature of crystalline H_2O ice, the abundance of crystalline H_2O ice is only based on the strength of the 43 μm peak and is in that sense accurate to about 1% of the total mass. However, if there is a very cool H_2O ice dust shell surrounding this object, which can be responsible for the LWS excess and missing strength of the 60 μm feature, the H_2O ice abundance would probably increase at least an order of magnitude.

We tried different models and only with large grains we were able to fit the shape, strength and position of the 10 μm feature. Smaller grain sizes (spherical or not) would produce a distinct and relatively sharp peak at shorter wavelengths in contrast to the flat spectrum we observed.

The presence of these large grains causes a grey extinction at optical wavelengths. This influences our previous determination of the extinction (see Sect. 3.1) and therefore the luminosity of both stars. The luminosity of the stars was derived using the standard interstellar extinction law (Fluks et al. 1994) for both the interstellar and circumstellar extinction. Since the colour excess changes much less when dealing with large grains, the stars are brighter than derived earlier in this paper. Using an iterative fitting scheme we re-derived the luminosity and interstellar extinction. We find a luminosity of $1.2 \times 10^4 d^2 L_{\odot}$ for the hot star and $6.8 \times 10^3 d^2 L_{\odot}$ for the cool star and an interstellar extinction of $E(B - V) = 1.1$ mag. Note that this value for the interstellar extinction is very close to the value which has been derived from the DIBs. Furthermore, our model predicts an optical depth to the star of $\tau = 0.6$ at 6583 \AA , which is in very good agreement with the value $\tau = 0.6 \pm 0.1$ found by van Loon et al. (in prep.) for the optical depth at [N II]-line. Although τ at 6583 \AA is 0.6, the circumstellar $E(B - V)$ is only 0.015 mag., due to the grey extinction (at optical wavelengths) of the large grains. So, the problem between the total extinction on one side and the circumstellar and interstellar dust extinction on the other side is resolved by the presence of large grains in the circumstellar environment leading to a non-standard extinction law for the dust shell.

Even with these large grains we were not able to fit the entire shape of the 10 μm silicate feature. Especially around 13 μm our models predicted lower flux levels than observed. When we subtract our model fit from the observations, a 13 μm feature is evident. This feature resembles the 13 μm feature observed in AGB stars with low mass loss rates, and is often attributed to corundum ($\alpha\text{-Al}_2\text{O}_3$) (Onaka et al. 1989; Begemann et al. 1997; Kozasa & Sogawa 1998). Therefore we also included corundum in our modelling, which indeed gives a much better fit around 13 μm .

The total mass in the shell, assuming a gas-to-dust ratio of 100 and a distance of 3.3 kpc, is $3.9 M_{\odot}$. Taking all the different errors and assumptions (such as the spherical shape of the dust grains) into account, this mass may be overestimated by up to a factor two.

While about 70 % of the dust shell consists of Fe-bearing amorphous olivines, about 7 to 15 %, depending on the assumed enstatite to forsterite ratio, constitutes of Mg-rich crystalline silicates. For the crystalline silicates only the end members of the olivine and pyroxene series, forsterite and enstatite respectively, are present. We note that the crystalline silicates only become important at the longer wavelengths. At $10 \mu\text{m}$ the amorphous silicates show a prominent peak but in this wavelength region there is no sign of the presence of the crystalline silicates. We conclude that the temperature of the crystalline silicates is lower than that of the amorphous ones. This temperature difference is confirmed by our model calculations. The temperatures at the inner radius are roughly 160, 125 and 100 K, for respectively the amorphous olivines, crystalline forsterite and the crystalline water-ice. These temperatures are higher than estimated in Sect. 4.2, but one should take into account that there is a temperature gradient and that the values mentioned here are maxima. The temperature difference is caused by the increased opacity in the UV, optical and near-IR when Fe is incorporated in the silicate. This implies that the two species are not thermally coupled, suggesting separate grain populations.

5.3. Discussion of the model fit

For some parts of the spectrum we did not obtain a satisfactory fit. The most obvious part is the LWS spectrum. We were not able to fit simultaneously the slope in the LWS part and the peak in the dust emission in the SWS part. A shallower density gradient would result in a broadening of the synthetic spectrum around $30 \mu\text{m}$. We decided to fit the peak instead of the long wavelength part, also because of the differences between the $100 \mu\text{m}$ IRAS and LWS flux in this region, which required the steep density gradient. Note that the model spectrum convolved with the IRAS $100 \mu\text{m}$ sensitivity gives a flux of 125 Jy, which is lower than both the IRAS and LWS flux. The fact that the flux in our model is too low and that the LWS spectrum contains a prominent and very cool H_2O ice band, gives an indication that an extra cool dust component, with likely a large amount of crystalline H_2O -ice, surrounding this object is required in the LWS beam. The presence of a large amount of crystalline H_2O , which is generally not found in the ISM, suggests that this extra contribution is due to a previous mass loss phase. The discrepancy between IRAS and ISO, however, remains unsolved. GKH had a 3 sigma detection of AFGL 4106 at 1.3 mm of 27 ± 9 mJy. In our model we find a flux of 17 mJy; this is within the errorbars. The ratio of 1.3 mm to (IRAS) $100 \mu\text{m}$ flux

densities is reproduced by our model, indicating that the largest grains are significantly smaller than $100 \mu\text{m}$.

Differences between the model and the broadband photometry in the optical and near-infrared, where we see the photospheres of both stars, can probably all be explained by the fact that we used blackbodies instead of real stellar photospheres. A third discrepancy is between 4.5 and $8 \mu\text{m}$. We were not able to fit this flat part of the spectrum. Part of it can be explained by photospheric CO absorption (around $4.5 \mu\text{m}$). A few experiments with FeO seem to indicate that a proper treatment of the shape effects of FeO might produce a flat spectrum in this area. On the other hand, the TIMMI N-band image shows a bright central emission, which cannot only be explained by the photospheres of the stars. It seems that an extra (hot) dust component is present at the center and that its infrared excess extends to the shorter wavelengths. Whether this represents a recent mass loss phase or a more stable circumstellar dust configuration (circumbinary disk) is unknown.

Previous modelling of AFGL 4106 has been performed by Volk and Kwok (1989) and HKV, who presented the same model, and GKH. Both models use in the center a single blackbody, with a temperature of 5000 (HKV) and 4750 K (GKH), surrounded by a single dust component circumstellar envelope. Because of these big differences between their and our model it is not useful to compare the inner radius and density at the inner radius found by them and us.

It is interesting that HKV and the present study both find a density distribution which differs from $\rho(R) \propto R^{-2}$, with R the distance of the position in the dust shell to the central object. HKV found a steeper density gradient than we did, but this is within the error margins. The main difference between our parameters and the ones of GKH is the exponent in the density gradient. Since we have now spectral coverage longwards of $25 \mu\text{m}$, we can exclude the possibility of a density gradient of $\rho \propto R^{-1}$. Their fit predicts a much broader IR excess around $25 \mu\text{m}$ than observed. It should be noted that GKH fit the IRAS 60 and $100 \mu\text{m}$ points better than the present study. However, because of the significant broadening of the top of the energy distribution when applying a flatter density distribution, which is not observed, the IR-excess problem is more likely solved with an extra dust shell. The density gradient of $\rho(R) \sim R^{-2.2}$ can be caused by two reasons: (I) The mass loss rate increased or (II) the outflow velocity decreased with time. In both cases the density gradient increases due to the geometric expansion of the dust shell with time. So whatever the reason is for the present steep gradient, it is intrinsic but has steepened during the expansion of the dust shell.

Assuming different grain size distribution for the different dust species might lead to an improvement of the fit and will result different mass ratios for the dust species.

A smaller size distribution for one dust component will result in a decrease of its mass ratio and vice versa.

6. Discussion

6.1. The distance and luminosity

In the literature distances ranging from 0.67 – 3.3 kpc (García-Lario et al. 1994) are given. However one should note that AFGL 4106 is located in the direction of Carina, so we are looking along a spiral arm, which makes it hard to relate column density and distance. Fortunately, we have spatial information from the N-band image. The inner radius of the dust shell is about 1.", and together with the expansion velocity found in CO (Josselin et al. 1998) and [NII]-line (van Loon et al., in prep.) of 30 to 40 km/s and the present-day shape of the SED, one can put a lower limit to its distance. Assuming that the outflow is spherical, which seems plausible according to our modelling results and the [N II]-line velocity distribution by van Loon et al. (in prep.), and that the velocity has not changed significantly in time, one can derive a kinematical age for the dust shell of 135 years times the distance in kpc. Due to the expansion of the dust shell it is expected that the circumstellar dust extinction becomes smaller, leading to an increase in the brightness at short wavelengths. AFGL 4106 has already been identified in the Cape Observatory Photographic Durchmusterung from 1895 to 1900 (Gill and Kapteyn 1900) with a photographic magnitude $M_{\text{pg}} = 9.9$ mag. In the Cordoba Durchmusterung (Thome 1914) a visual magnitude of 9.4 has been estimated for AFGL 4106. In the extended Henry Draper Catalogue, with observations taken between 1922 and 1937 (Cannon and Mayall 1949), its photographic magnitude was 10.0 ± 0.3 . On 18 March 1988 Hrivnak et al. (1989) measured a B magnitude of 10.24 ± 0.01 ($M_{\text{pg}} = M_{\text{B}} - 0.11$) and a V magnitude of 8.73 ± 0.01 . From these observations one can derive that $\Delta M_{\text{pg}} = 0.2 \pm 0.5$ mag. over the last 90 years and $\Delta M_{\text{V}} = -0.7 \pm 0.5$ mag. over the last 75 years, assuming an error of 0.5 magnitude in both Durchmusterungen. So the visual and photographic band trends contradict each other, although the errorbars are significant. Since the hot star is the dominant component at these two wavelengths it is possible that the star lowered its temperature, from a temperature with its peak luminosity at the photographic band to a temperature with its peak luminosity at the visual band. However, this is in contradiction with the present temperature, which peaks around the photographic band and is also not expected from evolutionary considerations.

In any case, the stability of the optical brightness of AFGL 4106 over a timescale of ≈ 90 years can be used to constrain its distance and luminosity. Using our dust model fit we can calculate the expected SED of the system and the visual and photographic brightness in the past, assuming that the dust composition, the outflow velocity, the temperature and the radii of the stars did not change.

For the photographic magnitude, it is safe to assume that the star has not brightened more than 0.3 magnitude over the last 90 years. This puts the star at a distance of at least 3.15 kpc and probably further away. On the other hand the brightening in the V-band over the last 75 years of $\Delta M_{\text{V}} = -0.7 \pm 0.5$ puts the star at a distance of $1.5_{-0.4}^{+2.1}$ kpc. There is only a very small overlap region between these two trends, suggesting a distance of 3.3 kpc, just at the upper limit quoted by García-Lario et al. (1994). The size of this overlap region is mainly based on the estimated errors of the Cape Observatory Photographic Durchmusterung and the Cordoba Durchmusterung.

This distance of 3.3 kpc implies that the luminosity is 1.3×10^5 and $7.4 \times 10^4 L_{\odot}$ for the hot and cool star respectively, again pointing to a massive binary system. Their luminosities point to stars with a main sequence mass between 15 and 20 M_{\odot} , using evolutionary tracks by Maeder & Meynet (1988). Other properties of AFGL 4106 also support the high masses of both stars. The expansion velocity of 30 to 40 km/sec is unusually high for AGB stars, and the relative large grains are typically found in the outflows massive supergiants (Jura 1996).

It is likely that the warm star is responsible for the expelled dust shell, and is now in the very rare evolutionary phase of the post-Red-Supergiants, which makes it a blue supergiant or WR star progenitor. Only a few other stars are in the same evolutionary status, e.g. IRC+10420 (Jones et al. 1993), and the central star of the radio nebula G79.29+0.46 (Trams et al. 1999).

6.2. The dust shell

At a distance of 3.3 kpc the mass loss episode took about 4.3×10^3 years and stopped 450 years ago. During this period the star expelled 3.9 M_{\odot} , assuming a gas to dust ratio of 100. This implies that the average mass loss rate is roughly $9. \times 10^{-4} M_{\odot}/\text{yr}$.

In our modelling we assumed spherical symmetry, but we do see substructure in our N-band images. This is also expected, since it is likely that the M-type supergiant will influence the spatial distribution of the dust and gas, expelled by the hot star, by transferring orbital momentum to the gas and dust. This effect can create a density enhancement in the plane of the binary. This possible enhancement can lead to an over- or under-estimate of the total mass, depending on the angle at which we observe this system. However, the shape of the [N II]-line derived from different rotation angles of the slit, suggest that the shape of the dust shell is close to a sphere (van Loon et al., in prep.). This implies that the orbital separation between the two stars is probably relatively large and therefore the influence of the companion on the mass-loss not so important. So, although the spherical symmetry and other assumptions used in our model calculations might be somewhat simple, it is not expected that the mass-loss

rate and the total mass found in our calculations would change more than a factor 2.

6.3. Formation of crystalline silicates

The formation of crystalline silicates is still largely unknown. Several researchers have tried to quantify the condensation sequence of oxygen rich dust (e.g. Tielens, 1990; Gail, 1998). However, these are mainly based on the different condensation temperatures, therefore assuming thermal equilibrium; it is not known if this assumption is valid. Condensation of dust species and chemical reactions will only occur if: (I) the density is high enough and (II) the temperature is suitable (low enough for condensation and high enough for chemical reactions). Since both the density and the temperature decrease with the distance from the star, it is likely that at a certain moment the dust structure freezes out. It is this stable dust configuration which we see at the moment. Taking the condensation sequences mentioned above, it is expected that the first silicate that will form is forsterite. When the temperature becomes lower and the density is still high enough this will transform into enstatite. Both species are expected to form above the glass temperature and are therefore thought to be crystalline. We see evidence in our spectrum for both forsterite and enstatite. This implies that the forsterite to enstatite transition is stopped before the forsterite was completely transformed. There might be 3 reasons for this: (I) The density became too low, (II) the temperature dropped too rapidly or (III) other chemical reactions took over. It is likely that it is a combination of these three. One chemical reaction that could take place at lower temperatures is the incorporation of Fe into the silicates. Since our spectra show that the crystalline silicates are very Mg- rich and the amorphous silicates contain a lot of Fe, it is likely that this incorporation of Fe results in a destruction of the crystal structure. The clear chemical separation between the amorphous and crystalline materials is intriguing. It appears that the inclusion of Fe in Mg-rich silicates is a kind of runaway process.

Tielens et al. (1998) proposed a scenario for such a chemical separation between amorphous and crystalline silicates. When the temperature becomes low enough Fe may react with the Mg-rich crystalline silicates. The opacity will increase, due to the incorporation of Fe, and therefore the temperature of the grain. This process will act as a thermostat, incorporating just sufficient Fe in the grains to keep the temperature near 800 K where Fe can just diffuse in. This temperature is below the glass temperature for Fe-bearing silicates and the lattice cannot attain its energetically most favorable structure, thus leading to an amorphous structure. Because of the increased opacity due to the incorporation of Fe, it is likely that the temperature of the other grains behind this Fe-reaction zone will decrease, leading to an even higher difference between the Fe-rich (amorphous) and Mg-rich (crystalline) silicates if

thermal coupling between gas and dust can be neglected. Grains that already contain a small amount of Fe will be hotter and therefore the reaction rate for the adsorption of Fe will be higher than for grains without any Fe. This would lead to the required runaway process. If this scenario is correct, it would imply that the crystalline silicates are the primordial condensation products, and this will give us new insights in the dust nucleation. Although this would lead to the required chemical separation between the crystalline and amorphous materials, it is not clear why the amorphous olivines should contain more Fe than the amorphous pyroxenes, if present at all.

Besides the forsterite-enstatite condensation sequence, Tielens (1990) also presented a condensation sequence starting with corundum. The next condensation product would then be melilite, for which we find some evidence. According to the same scheme diopside would form. Since certain strong features of this material are not found in our ISO-spectrum, this may imply that the dust forming process along this condensation sequence line froze out around amorphous melilite.

Gail and Sedlmayr (submitted to A&A) applied non-equilibrium calculation for the dust formation in outflows of M stars. They do explain the formation of several dust species, such as the amorphous Fe-rich olivines, however they do not consider, based on laboratory experiments, the formation of pyroxenes and are not capable to explain the co-existence of pure forsterite particles and Fe-rich amorphous olivines.

7. Conclusions

The main results of this study can be summarized as follows:

- 1 AFGL 4106 is a (double-lined spectroscopic) binary, consisting of a warm star with $T_{\text{eff}} = 7250$ K and a cool companion with $T_{\text{eff}} = 3750$ K.
- 2 The luminosity ratio of both stars $L_{\text{warm}}/L_{\text{cool}} = 1.8$, which indicates that both stars are evolved. The warm star is likely responsible for the dust shell.
- 3 The expansion velocity of the shell, the grain size distribution and the minimal variations in the photographic and V band over the last 90 years all suggest a high luminosity. We conclude that the stars are at 3.3 ± 1.0 kpc and have $L/L_{\odot} = 1.3 \times 10^5$ and 7.4×10^4 respectively. These values correspond to main sequence masses of 15 to 20 M_{\odot} . The warm star is probably evolving rapidly to the blue part of the HR-diagram and may evolve to a blue-supergiant (ending its life like SN 1987A) or to a Wolf-Rayet phase.
- 4 The main component of the dust are large ($\approx 1\mu\text{m}$) amorphous, Fe-rich olivines. If also amorphous pyroxenes are present, they will have a much lower Fe content. We find a rich spectrum of narrow solid state emission bands in the ISO-SWS and LWS spectra,

which we identify with crystalline olivines and pyroxenes. These grains are Mg-rich and Fe-poor and have an abundance between 7 and 15 % by mass, depending on the assumed enstatite to forsterite ratio. We also find evidence for the presence of FeO, Al₂O₃, melilite and crystalline H₂O-ice. Shape effects can have an important influence on the derived abundances.

- 5 The temperatures for the different dust species are quite different, this is caused by variations in their absorption characteristics at visual and near-IR wavelengths. These temperature differences imply that the different dust species are not thermally coupled, directly (e.g. as a composite grain) nor indirectly (e.g. via gas-dust interactions).
- 6 The crystalline silicate bands can be divided into narrow (FWHM/ $\lambda < 0.03$) and broad (FWHM/ $\lambda > 0.03$) features. The wavelengths of the broad features match well with forsterite, while those of most of the narrow features line up well with enstatite. The width of the features is significantly smaller than those observed in laboratory spectra. The abundance ratio of enstatite to forsterite is between 3 and 1.
- 7 The mean mass-loss rate was $\approx 9. \times 10^{-4} M_{\odot}/\text{yr}$ for a period of about 4.3×10^3 years and probably increased during this period. The mass loss stopped 450 years ago. The total mass expelled, assuming a gas to dust ratio of 100, is $3.9 M_{\odot}$.
- 8 We find a cool dust component, which cannot be fitted by our dust model. This component is either an older mass loss phase, or an incorrect background subtraction of the ISM. We also found indications from the spectrum between 4 and 7 μm and the 10 μm imaging that a third dust component, close to the binary is present. Whether this represents a recent mass loss phase or a more stable circumstellar dust configuration is not known.

Because of its (IR-)brightness AFGL 4106 will be a key object in the further study of (crystalline) dust formation. High resolution imaging and spectroscopy both in the optical and IR will allow us to constrain the circumstellar versus interstellar extinction, the photospheres of the components, density and abundance gradients through the CSE, and thus the conditions for dust formation and evolution.

Acknowledgements. The authors wish to thank the SWS Instrument Dedicated Team, in particular Th. de Graauw, for their support in obtaining the spectra. We thank A.G.G.M. Tielens for fruitful discussion. FJM acknowledges support from NWO grant 781-71-052. LBFMW, AdK and JB acknowledge financial support from the Royal Netherlands Academy of Arts and Sciences, and from an NWO 'Pionier' grant.

References

Barlow M.J., 1998, A&SS 255, 315

- Begemann B., Dorschner J., Henning Th., et al., 1997, ApJ 476, 199
- Bertie J.E., Labbé H.J., Whalley E., 1969, The Journal of Chemical Physics 50, 4501
- Bohren C.F., Huffman D.R., 1983, Absorption and scattering of light by small particles., John Wiley and Sons, Inc., New York
- Bouwman J., Waters L.B.F.M., 1998, A&SS 255, 435
- Bruggeman D.A.G., 1935, Ann. Physics (Leipzig) 24, 636
- Cannon A.J., Mayall M.W., 1949, Ann. Astron. Obs. Harvard Coll. 112, 1
- Clegg P.E., Ade P.A.R., Armand C., et al., 1996, A&A 315, L38
- Decin L., Cohen M., Eriksson K., et al., 1997, in Proceedings of the First ISO Workshop on Analytical Spectroscopy with SWS, LWS, PHT-S and CAM-CVF, ed. Heras A.M., Leech K., Trams N.R., Perry M., ESA Publications Division, Noordwijk, The Netherlands
- Dorschner J., Begemann B., Henning Th., et al., 1995, A&A 300, 503
- Ehrenfreund P., Cami J., Dartois E., Foing B.H., 1997, A&A 317, L28
- Fluks M.A., Plez B., The P.S., et al., 1994, A+AS 105, 311
- Gail H.-P., 1998, A&A 332, 1099
- García-Lario P., Manchado A., Parthasarathy M., Pottasch S.R., 1994, A&A 285, 179
- García-Lario P., Manchado A., Pych W., Pottasch S.R., 1997, A&AS 126, 479
- Gill D., Kapteyn J.C., 1900, Ann. Cape Obs. Edinburgh, vol. V
- de Graauw Th., Haser L.N., Beintema D.A., et al., 1996, A&A 315, L49
- Gürtler J., Kömpe C., Henning Th., 1996, A&A 305, 878
- Henning Th., Mutschke H., 1997, A&A 327, 743
- Henning Th., Begemann B., Mutschke H., Dorschner J., 1995, A&AS 112, 143
- Herbig G.H., 1995, ARA&A 33, 19
- Hrivnak B.J., Kwok S., Volk K.M., 1989, ApJ 346, 265
- IRAS explanatory supplement 1988, eds. C. Beichmann, et al.
- Jäger C., Molster F.J., Dorschner J., et al., 1998, A&A 339, 904
- Jenniskens P., Désert F.-X., 1994, A&ASS 106, 39
- Jones T.J., Humphreys R.M., Gehrz R.D., et al., 1993, ApJ 411, 323
- Josselin E., Loup C., Omont A., et al., 1998, A&AS 129, 45
- Jura M., 1996, ApJ 472, 806
- Käufel H.-U., Jouan R., Lagage P.O., et al., 1994, Infrared Phys. Technol. 35, 203
- Kessler M.F., Steinz J.A., Anderegg M.E., et al., 1996, A&A 315, L27
- Koike C., Shibai H., 1998, ISAS report no. 671
- Koike C., Shibai H., Tuchiya A., 1993, MNRAS 264, 654
- Koike C., Kaito C., Yamamoto T., et al., 1995, Icarus 114, 203
- Kozasa T., Sogawa H., 1998, A&SS 255, 437
- Kurucz R.L., 1991, in Precision Photometry: Astrophysics of the Galaxy, Ed. Davis Philip A.G., Uppgren A.R., Janes K.A., L. Davis Press, Schenectady
- Little-Marenin I.R., Little S.J., 1988, ApJ 333, 305
- Little-Marenin I.R., Little S.J., 1990, AJ 99, 1173
- Lucy L.B., 1974, AJ 79, 745
- Maeder A., Meynet G., 1988, A&AS 76, 411

- Mathis J.S., Rumpl W., Nordsieck K.H., 1977, ApJ 217, 425
Monnier J.D., Geballe T.R., Danchi W.C., 1998, ApJ 502, 833
Mutschke H., Begemann B., Dorschner J., et al., 1998, A&A 333, 188
Omont A., Forveille T., Moseley S.H., et al., 1990, ApJ 355, L27
Onaka T., de Jong T., Willems F.J., 1989, A&A 218, 169
Schaeidt S.G., Morris P.W., Salama A., et al.: 1996, A&A 315, L55
Scott A., Duley W.W., 1996, ApJS 105, 401
Servoin J.L., Piriou B., 1973, Phys. Stat. Sol. (b) 55, 677
Steyer T.R., 1974, PHD-thesis, University of Arizona
Swinyard B.M., Clegg P.E., Ade P.A.R., et al., 1996, A&A 315, L43
Tielens A.G.G.M., 1990, in From Mira's to Planetary Nebulae: Which path for stellar evolution?, eds. M.O. Mennessier & A. Omont, 186
Tielens A.G.G.M., Waters L.B.F.M., Molster F.J., Justtanont K., 1998, A&SS 255, 415
Thome J.M., 1914, Results of National Argentine Obs. 21, 1
Trams N.R., Van Tuyl C.I., Voors R.H.M., et al., 1999 in IAU Colloquium 169, Variable and Non-spherical stellar winds in luminous hot stars", Eds. Wolf, Fullerton, Stahl
Valentijn E.A., Feuchtgruber H., Kester D.J.M., et al., 1996, A&A 315, L60
Volk K.M., Kwok S., 1989, ApJ 342, 345
Waters L.B.F.M., Molster F.J., de Jong T., et al., 1996, A&A 315, L361
Waters L.B.F.M., Waelkens C., van Winckel H., et al., 1998, Nat 391, 868